Dwarf galaxy star formation histories in Local Group cosmological simulations

by

Ruth A. R. Digby
B.Sc., University of Victoria, 2016

A Thesis Submitted in Partial Fulfillment of the
Requirements for the Degree of

MASTER OF SCIENCE

in the Department of Physics and Astronomy

Dwarf galaxy star formation histories in Local Group cosmological simulations

by

Ruth A. R. Digby
B.Sc., University of Victoria, 2016

Supervisory Committee

Dr. J. F. Navarro, Supervisor
(Department of Physics and Astronomy)

Dr. A. McConnachie, Departmental Member
(Department of Physics and Astronomy)

ABSTRACT

Dwarf galaxies are powerful tools in the study of galactic evolution. As the most numerous galaxies in the universe, they probe a diverse range of environments: some exist in near-isolation, allowing us to study how a galaxy's evolution depends on its intrinsic properties. Others have been accreted by larger galaxies and show the impact of environmental processes such as tidal stripping. Because dwarf galaxies have shallow potential wells, these processes leave strong signatures in their star formation histories (SFHs).

We use state-of-the-art cosmological hydrodynamical simulations to study the evolution of dwarf galaxies in Local Group analogues. Their SFHs are remarkably diverse, but also show robust average trends with stellar mass and environment. Low-mass isolated dwarfs ($10^5 < M_*/M_\odot < 10^6$) form all of their stars in the first few Gyr, whereas their more massive counterparts have extended star formation histories, with many of the most massive dwarfs ($10^7 < M_*/M_\odot < 10^9$) continuing star formation until the present day. Satellite dwarfs exhibit similar trends at early and intermediate times, but with substantially suppressed star formation in the last ~ 5 Gyr, likely as a result of gas loss due to tidal and ram-pressure stripping after entering the haloes of their primaries.

These simple mass and environmental trends are in good agreement with the derived SFHs of Local Group dwarfs whose photometry reaches the oldest main sequence turnoff. SFHs of galaxies with less deep data show deviations from these trends, but this may be explained, at least in part, by the large galaxy-to-galaxy scatter, the limited sample size, and the large uncertainties of the inferred SFHs.

Contents

List of Tables

List of Figures

Acknowledgements

I am deeply grateful to my family and friends for all of their love and support over the years. Without you, I would not be the person I am today, and I would certainly not have written this thesis.

A few people are owed particular thanks for their role in this work:

Kristi Webb, Jacqui Irvine and Megan Tannock, the Babe Brigade, for years of laughter and love. I'm lucky to know you all.

Brittany Howard and Mallory Thorp, the best academic family I could ask for, for colloquium knitting, thesis writing, and emotional support.

Azi Fattahi, for her immeasurable patience and advice when I first started research, and for her collaboration on the work presented in this thesis.

Julio Navarro, for the academic guidance and opportunities these past two years.

Dedication

To my parents,
for instilling me with their love of learning,

and to Nic Loewen,
for all the silly faces.
See what you've done?

Chapter 1

Introduction

Dwarf galaxies, defined as those which are hundreds or thousands of times less massive than our Milky Way, are powerful tools in the study of galactic evolution on all scales. As the most numerous galaxies in universe, they probe a diverse range of environments and are exposed to a correspondingly diverse array of physical processes. Because of their low masses and shallow potential wells, these processes leave strong signatures in their star formation histories (SFHs), forming a 'fossil record' that holds clues to their evolutionary histories.

The observational study of dwarf galaxy evolution is extremely challenging. It is hampered by systematics, by our inability to directly measure quantities of interest, and, most fundamentally, by the requirement to infer a galaxy's lifetime evolution from observations taken at a single snapshot in time. Nonetheless, remarkable progress has been made thanks to innovations both in theoretical methodology (determining SFHs through modelling of colour-magnitude diagrams) and in telescope capabilities. There are now uniformly reduced SFHs for approximately 100 dwarf galaxies in our local neighbourhood. Of these, $\sim 26\%$ have sufficiently deep observations to robustly constrain early periods of star formation.

One the computational front, advances in numerical methodology have enabled simulations of unprecedented resolution, both on cosmological scales (simulating large regions of the universe from primordial density perturbations to the present day) and on individual galaxy scales (idealized simulations that start from a pre-made galaxy and study its response to perturbations).

Despite this progress, however, limited effort has been expended in the theoretical study of dwarf galaxy SFHs. Most SFH studies have been at the group and cluster scale, measuring the SFHs of galaxies much larger than dwarfs; on the other hand, most studies of dwarf galaxy evolution have been in small simulations that lack cosmological context or environmental influences.

My work aims to fill this gap: by studying the SFHs of dwarf galaxies in cosmological simulations, we can determine how internal and environmental factors impact the evolution of dwarf galaxies, and contribute to a more comprehensive theoretical framework for the physics of galaxy evolution at all scales.

The remainder of this chapter introduces the context in which my research takes place. Our current cosmological model, and its predictions for dwarf galaxies, are described in Sections 1.1 and 1.2. Section 1.3 provides a brief overview of galaxy evolution at dwarf scales. Section 1.4 describes how SFHs are being used to study this evolution. Finally, Section 1.5 provides a roadmap to the rest of this thesis.

1.1 Cosmological Context

Our current 'standard model' of cosmology is Λ Cold Dark Matter (ΛCDM). In ΛCDM, dark matter - non-baryonic, collisionless material with a very low thermal velocity - dominates over regular baryonic matter by roughly a factor of $5:1$ (Planck Collaboration et al., 2018). Dark and baryonic matter together make up only $\sim 32\%$ of the universe's mass-energy budget; the rest is comprised of dark energy. The nature of dark energy is not presently understood, but it behaves much like Einstein's cosmological constant (the 'Λ' of ΛCDM), providing a form of negative pressure responsible for the accelerating expansion of the universe.

Strucure in ΛCDM grows hierarchically (White & Rees, 1978; White & Frenk, 1991). Quantum density fluctuations in the early universe are amplified by gravity until they are sufficiently overdense to decouple from the expansion of the universe, at which point they gravitationally collapse. Overdense regions collapse into sheets, the intersections of sheets collapse into filaments, and the intersections of filaments into dense nodes and halos. The resulting large-scale structure of the universe is the 'cosmic web,' a network of dark matter sheets and filaments punctuated by large voids (see, e.g., Cautun et al., 2014, and references within).

At highly non-linear scales within the cosmic web, dark matter halos form from the gravitational collapse of overdense regions. These halos then grow through a combination of accretion and the merging of smaller halos. As a result, dark matter halos contain rich substructure in the form of accreted subhalos.

It is within these halos and subhalos that galaxies form. Baryonic material follows the gravitational potential induced by the dominant dark matter. As gas cools and flows in to halos, it is able to condense and form stars. The mass of galaxy that forms depends on the host halo mass, as described by the stellar mass - halo mass (SMHM) relation (Figure 1.1). In the following section, we outline ΛCDM's predictions for the mass functions of dwarf galaxies and their host halos, and describe some tensions with ΛCDM that have arisen from observational estimates of the SMHM relation.

1.2 Cosmological Predictions for Dwarf Galaxies

1.2.1 Mass Functions of Halos and Galaxies

ΛCDM makes clear predictions for the mass function of dark matter halos. As a result of hierarchical assembly, the number density of halos is expected to decrease monotonically with increasing halo mass (e.g. Jenkins et al., 2001; Murray et al., 2013).

The galaxy stellar mass function, which can be measured through observational surveys, takes a similar form. Low-mass (dwarf) galaxies are far more abundant than their more massive counterparts. Carried along by the hierarchical assembly of the dark matter halos in which they reside, galaxies grow through both accretion and merging, and many dwarf galaxies are found as satellites of larger systems.

Although both mass functions are monotonically decreasing, the low-mass end of the galaxy stellar mass function is shallower than that of the halo mass function, meaning that there are far more low-mass halos than there are low-mass galaxies. As a result, the SMHM becomes very steep, as demonstrated in Figure 1.1. A small range in halo masses can correspond to a decade or more in stellar mass. Indeed, all galaxies with stellar masses below $\sim 10^7 \mathrm{M}_\odot$ form in halos of approximately the same mass.

1.2.2 The SMHM Relation and Tensions in ΛCDM

Observations of the faint end of the SMHM relation provide a useful test of ΛCDM at small scales (e.g., Read et al., 2017). The observed galaxy mass function can be compared to a theoretical halo mass function through abundance matching, and to an 'observed' halo mass function by using observational proxies to estimate the masses of galaxies' halos. Both of these approaches are described below. If the resulting 'theoretical' and 'observed' SMHM relations are inconsistent, this implies that our understanding of dwarf galaxy formation in ΛCDM may be incomplete.

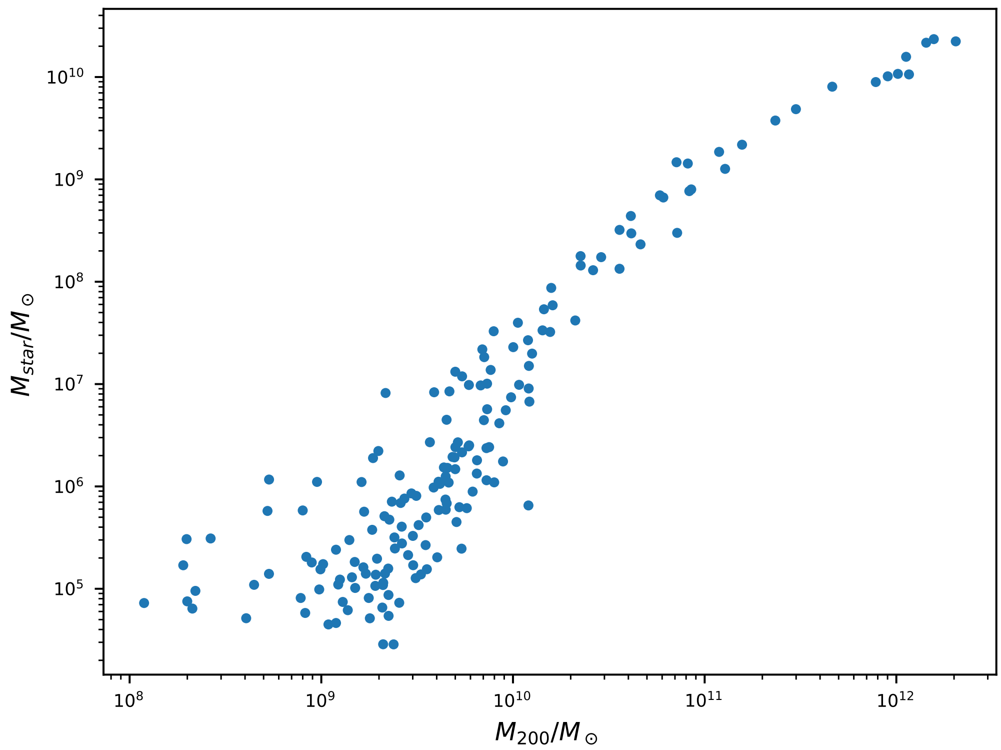

Figure 1.1: The SMHM relation for centrals (field dwarfs and primaries) in the APOSTLE simulation. Note the 'knee' at halo masses $M_{200} \sim 10^{11}\mathrm{M}_\odot$, and the steepness of the SMHM relation below this knee. As a result, a small range in halo masses can correspond to a decade or more in stellar mass; for example, the range $10^9 M_{200}/\mathrm{M}_\odot < 2 \cdot 10^9$ corresponds to $2 \cdot 10^4 M_*/\mathrm{M}_\odot < 10^7$.

Abundance matching (e.g. Kravtsov et al., 2004; Guo et al., 2011; Behroozi et al., 2013) compares the stellar masses of observed galaxies to halo masses predicted by dark matter only (DMO) simulations. The two populations are sorted by mass and then matched, galaxy-to-halo, according to their rank. This results in a 'theoretical' SMHM relation.

Observational estimates of halo masses rely on tracers such as galactic velocity dispersions or HI rotation curves. Converting these into halo masses requires knowledge of the dark matter density profile within the galaxy, which is often assumed to obey a 'cuspy' NFW profile (Navarro et al., 1996) or a more 'cored' profile with a lower central density. ΛCDM predicts cuspy profiles, but baryon interactions may (Zolotov et al., 2012) or may not (Fattahi et al., 2016a) affect this distribution.

Taken at face value, local observations suggest tensions with ΛCDM. The number of dark matter subhalos, massive enough to host dwarfs, that are predicted to surround galaxies like the Milky Way and Andromeda outnumbers the observed satellites by roughly an order of magnitude (the Missing Satellites (MS) problem; Klypin et al., 1999; Moore et al., 1999).

This discrepancy can be partially resolved if galaxies do not form in halos below some threshold mass. This threshold could be set by cosmic reionization (Efstathiou, 1992; Thoul & Weinberg, 1996; Benson et al., 2002; Dawoodbhoy et al., 2018, see also Section 1.3). However, the presence of low-mass "dark halos" – or, simply, galaxies that are too faint to be easily identified in existing surveys – may be insufficient to resolve the discrepancy. The Milky Way's satellites would be expected to inhabit its most massive subhalos; however, kinematic estimates of the satellites' host halo masses are significantly lower than the massive halos predicted by dark matter simulations (the Too Big To Fail (TBTF) problem; Boylan-Kolchin et al., 2011). Some studies (e.g. Fattahi et al., 2016a; Read et al., 2017) have suggested that the MS and TBTF problems may be resolved by accounting for baryonic effects and uncertainties in observational estimates; however, the literature has not reached a consensus on this matter.

Dwarf galaxies therefore remain an area of great interest, as it is in the dwarf galaxy regime that tensions with ΛCDM appear. The physical processes regulating star formation at these masses are of particular interest.

1.3 Galactic Evolution at the Low-Mass End

A very simplistic picture of galactic evolution can be laid out as follows.

As described above, dark matter density fluctuations in the early universe first expand during inflation, then collapse under gravity, and form dark matter halos into which gas flows.

Quite early in the universe (perhaps as early as $z_{reion} = 10.6$ (Komatsu et al., 2011) or as late as $z_{reion} = 5.3$ (Glazer et al., 2018; Planck Collaboration et al., 2018)), ultraviolet radiation from the first stars and galaxies heated gas to the ionization temperature of hydrogen ($\sim 10^4 K$). This heating evaporated the gas from any halos with virial temperatures below this value. Over time, gas could cool back into the halo, but frequently it is lost to environmental effects such as stripping by the cosmic web (e.g., Benítez-Llambay et al., 2015).

The end result of cosmic reionization depends both on a halo's mass and on the state of its baryons at z_{reion}. In low-mass halos that had not begun forming stars, gas loss from reionization prevents star formation from ever beginning. This explains the 'dark halos' invoked to explain the Missing Satellites problem (Section 1.2.2). In those halos where some gas had cooled sufficiently to begin forming stars, star formation continued until the cold gas was depleted, and star formation ceased. In some cases, star formation may be reignited if such a galaxy accretes sufficient gas (Benítez-Llambay et al., 2015; Ledinauskas & Zubovas, 2018; Wright et al., 2019).

Galaxies continue to grow through a combination of accretion and mergers. As stars form and evolve, they release energy via supernovae and stellar winds. This energy heats the surrounding gas, and may be sufficient to drive it out of the galaxy entirely, inhibiting further star formation. This is particularly significant in low-mass galaxies, whose shallow potential wells are insufficient to retain gas heated by stellar feedback.

Dwarf galaxy evolution can also be drastically altered by interactions with the environment. These effects are most significant in dwarfs which have been accreted into the halos of larger galaxies, becoming satellites. However, even isolated dwarfs can interact with environmental features such as dense gaseous filaments of the cosmic web.

Ram pressure stripping (Gunn & Gott, 1972; McCarthy et al., 2008; Tonnesen & Bryan, 2009; Emerick et al., 2016) occurs when a galaxy moves quickly through a dense gaseous region (such as the gaseous halo of a larger galaxy, or a cosmic web filament). The gaseous halo of the travelling galaxy feels a pressure induced by hydrodynamical interaction with the medium through which it is passing. If this pressure exceeds the restoring force tying the gaseous halo to its galaxy, the gas can be stripped away. Ram pressure stripping primarily removes hot gas, rather than cool dense gas which has already cooled into the galaxy's centre. Stars are unaffected by ram pressure stripping.

Tidal stripping (Mayer et al., 2001; Kravtsov et al., 2004; Peñarrubia et al., 2008) occurs when a galaxy experiences differential gravitational forces across its body, induced by passing near to a much larger object. This differential gravitational force strips material from the smaller galaxy. Tidal stripping primarily affects dark matter (Smith et al., 2016; Fattahi et al., 2018), leaving stars largely unaffected.

1.4 Studying Star Formation Histories

Dwarf galaxies exhibit a remarkable degree of diversity. Traditionally, this diversity has been classified in terms of morphology, with dwarfs categorized as either dwarf spheroidals (dSphs) or dwarf irregulars (dIrrs) (Hodge, 1971). dSphs are gas-poor and quiescent (non-star-forming); dIrrs are gas-rich and actively forming stars. Additional categories have been added as more diversity has been observed: the 'transition' (dT) systems have recent star formation but no massive stars or HII regions; ultra-faint dwarfs (UFDs) have stellar masses below $10^5 \mathrm{M}_\odot$ and correspondingly low surface brightness; ultracompact dwarfs (UCDs) are centrally-concentrated and star-forming, and may be more akin to globular clusters than typical dwarfs (see, e.g., the review by Tolstoy et al., 2009, and references therein).

However practical this classification may be from an observational standpoint, it contains little physical insight on the evolutionary processes a dwarf has undergone. Morphology is a transient state, and morphology-based classifications are heavily weighted by a galaxy's most recent past. Indeed, many dSph and dIrr systems share structural properties and evolutionary characteristics, and only differ because star formation has ceased (often quite recently) in the former (Grebel, 1999; Tolstoy et al., 2009; Weisz et al., 2011; Gallart et al., 2015).

Galactic evolution is better studied through the analysis of lifetime star formation histories (SFHs). The processes described in Section 1.3 all impact the ability of galaxies to form stars, enhancing or suppressing the star formation rate (SFR), and in some case extinguishing star formation altogether. The lifetime SFH of a galaxy therefore forms a fossil record of its evolution. Low-mass dwarfs, with their shallow potential wells, are particularly susceptible to all of these processes and are left with correspondingly strong signatures in their SFHs.

The observational study of dwarf SFHs is an active field. SFHs can be derived for nearby dwarfs by comparing their colour-magnitude diagrams (CMDs) to stellar evolution models, a process described in detail in Section 3.1. This approach has been in use since 1989 (Ferraro et al., 1989; Tosi et al., 1989), but only in recent years have large catalogues of uniformly-reduced SFHs been published (Weisz et al., 2011, 2014; Gallart et al., 2015; Skillman et al., 2017). This homogeneity is crucial for SFH comparisons, as SFH derivation is prone to large systematic uncertainties.

These observations have yielded a startling diversity of SFHs, even amongst dwarfs with similar present-day characteristics. This has elicited a number of questions that so far have not been satisfactorily answered. One of these is the role of the environment. Although there are clear overall trends – nearly all satellites of the Milky Way and M31 are quiescent dSphs, and nearly all isolated dwarfs are star-forming dIrrs (Geha et al., 2012) – there are puzzling exceptions. The dSphs Cetus and Tucana, for instance, are isolated yet quiescent (Monelli et al., 2010a,b). Another question is the role of galaxy mass: observed SFHs show no obvious dependence on the stellar mass of the dwarf. Is this because trends are weak and easily masked by large galaxy-to-galaxy scatter and the still relatively small number of systems surveyed, or a result of deeper physical significance?

Finally, the sheer diversity of SFHs is a puzzle in itself: what drives galaxies with similar stellar masses, presumably inhabiting similar mass haloes, and in similar environments, to exhibit the bewildering array of evolutionary histories their CMDs suggest?

Despite the activity on the observational front, and the questions that have arisen from it, there have been relatively few theoretical studies directly targeting dwarf galaxy SFHs. This is due in part to the computational challenge of simulating dwarf galaxy evolution in Local Group-like environments. Because of the difference in scales between dwarfs and their hosts, it can be prohibitively expensive to simulate dwarfs at resolutions high enough to probe the physics governing their star formation histories while simultaneously including the spatial and dynamical scales of a Milky Way - sized halo. Detailed studies of dwarf galaxies therefore tend to focus on isolated, low mass halos (Hopkins et al., 2014; Fitts et al., 2017), or very small samples of Milky Way-like satellite systems (Okamoto et al., 2010; Zolotov et al., 2012; Wetzel et al., 2016; Buck et al., 2018).

These studies have explored the effects of energetic feedback, ram pressure and tidal stripping, and related physics on gas content, kinematics, morphology, and adherence to global scaling relations. Few authors have investigated the impact of these physical processes on galaxies' SFHs. Of those that have, many limit their discussion to 'quenching,' the total cessation of star formation. Wetzel et al. (2015) derived quenching timescales for Local Group dwarfs by combining Local Group observations with estimated infall times from the ELVIS DMO simulation. They found that low-mass galaxies quench fastest, and that quenching timescales peak for galaxies with $M_* \sim 10^9 \mathrm{M}_\odot$. Simpson et al. (2018) studied the quenched fraction and gas content of satellites in the Auriga suite of Milky Way-like halos. They found clear trends with mass and distance: 90% of systems with $M_* < 10^6 \mathrm{M}_\odot$ were quenched regardless of their distance from the MW analogue, and at higher masses, quenched fraction was inversely correlated with distance. HI-poor satellites followed similar trends, and ram pressure stripping was identified as the dominant quenching mechanism.

Detailed lifetime star formation histories have been studied by Benítez-Llambay et al. (2015), who investigated the impact of cosmic reionization on isolated dwarfs using the CLUES Local Group simulation. Their dwarfs were characterized by great SFH diversity, and included a sample of dwarfs with 'double-peaked' SFHs marked by quiescence at intermediate times ($t \sim 4 - 8$ Gyr), which they attributed to cosmic reionization. In a similar vein, Ledinauskas & Zubovas (2018) and Wright et al. (2019) used semi-analytic models and cosmological simulations of isolated dwarfs, respectively, to investigate whether star formation could be reignited in previously-quenched dwarfs.

However, a detailed analysis of how dwarf galaxy star formation histories depend on internal and external physical drivers has not been undertaken[1]. This thesis details my research to that end.

1.5 Thesis Outline

In this project I use the cosmological simulations APOSTLE and Auriga to characterize the star formation histories of dwarf galaxies, and to investigate how the evolution of

---

[1] Following the publication of the results presented in Chapters 2-4, Garrison-Kimmel et al. (2019) submitted a paper investigating these questions in the FIRE simulation. At the time of writing, their paper had yet to be accepted, but we compare our results with their preliminary findings in Chapter 4.

dwarf galaxies depends on their stellar mass and environment. These results are compared with star formation histories derived from HST observations of dwarf galaxies in and around the Local Group.

Chapter 2 introduces the simulations used in this work. Chapter 3 describes the process of deriving star formation histories from resolved CMDs, and introduces the sample of observations we use. The main results of the project - the dependence of dwarf galaxies on mass and environment - are presented in Chapter 4. The physical origins of these trends are explored in Chapter 5. Finally, we summarize our findings and propose avenues for further research in Chapter 6.

The research presented in Chapters 2-4 has been published as Digby et al. (2019).

Chapter 2

Numerical Techniques and Analysis

The simulated galaxies studied in this project were drawn from the APOSTLE and Auriga projects. Both APOSTLE and Auriga are ΛCDM cosmological hydrodynamical zoom-in simulations, but they run on fundamentally different types of code, and differ in their treatment of subgrid physics. This class of simulations, and the specific details of APOSTLE and Auriga, are described in the following sections.

2.1 Introduction to Cosmological Simulations

One of the most powerful tools in modern astrophysics is our ability to explicitly model galaxy evolution in a cosmological context. Numerical simulations allow us to start from a collection of dark matter and gas and, by solving the equations of gravity and hydrodynamics over time, produce a model universe in excellent agreement with our own.

This is a tremendous computational undertaking, due especially to the immense dynamic range involved. Many of the physical processes that govern star formation efficiency, such as supernova feedback, stellar outflows, and giant molecular cloud disruption by turbulence, shear, and tidal forces, operate at parsec scales or below. On the other hand, environmental impacts such as cosmic web-induced torque and galactic merger histories act on kpc and Mpc scales.

Numerical simulations fall into two basic classes. Dark matter only (DMO) simulations are the most computationally straightforward. They are extremely valuable for capturing large-scale physics such as the cosmic web, since baryons are irrelevant on those scales; they have also been used to great effect on small scales when paired with semi-analytic models. Hydrodynamical simulations, which incorporate baryons, are much more expensive but allow us to study the physics governing the visible universe.

Hydrodynamical simulations can be considered an extension of DMO simulations. We will thus first describe the basics of cosmological simulations as applied to DMO simulations, then describe the additional physics required to implement hydrodynamics.

2.1.1 Dark Matter Only Simulations

The observed universe is homogeneous when averaged over large scales. It is therefore possible to generate a cosmologically representative volume by simulating a reasonably large box with periodic boundaries. The box is filled with dark matter particles, and seeded with density fluctuations in the form of a Gaussian random field with a linear power spectrum consistent with CMB observations.

Dark matter is modelled by collisionless particles that interact only through gravity. Nominally this makes solving the equations of motion an $\mathcal{O}(N^2)$ problem, where N is the number of particles, but methods such as tree algorithms can reduce this to $\mathcal{O}(N \log N)$. Forces are not computed directly when particles are within a chosen force softening length of each other, in order to prevent excessively high values when particles get close together. The ratio of this softening length to the simulation's box size is often used as a measure of the simulation's dynamic range.

The largest dark matter only simulations to date have $\sim$ 10 billion particles (Springel et al., 2005), with particle masses $8.6 \times 10^8/h$ $\mathrm{M}_\odot$. This corresponds to a remarkable dynamic range, but the resolution is too low to study galactic evolution at the dwarf galaxy scale.

In order to study smaller-scale evolution while retaining the influences of a cosmologically representative volume, many simulations make use of the 'zoom-in' technique developed by Katz & White (1993). In this method, a large box is first simulated at relatively low resolution to capture the average behaviour of the universe. Regions of interest are then selected and re-simulated at higher resolution, with the low-resolution surroundings providing large-scale gravitational effects.

In hydrodynamical zoom-in simulations, which we describe in the next section, only the high-resolution region is simulated with baryons. The large, low-resolution box remains DMO.

2.1.2 Hydrodynamical Simulations

Simulations of the visible universe require the addition of hydrodynamics to model gas and stars. This poses a much greater computational challenge than DMO simulations do. Modelling baryonic fluids introduces the calculation of pressure forces and internal energy, as well as numerical prescriptions to handle shocks, turbulence, radiative transport, and other computationally expensive processes.

Regardless of how high a simulation's resolution may be, many physical processes will operate at sub-resolution scales that cannot be directly simulated. This 'subgrid physics' is instead approximated by semi-analytic recipes. These prescriptions are physically motivated, but the exact implementation can be somewhat arbitrary (see, e.g., review by Somerville & Davé, 2015). A detailed review of subgrid implementation is beyond the scope of this thesis, but some specific examples are given in Section 2.2.

Stars, like dark matter, are represented by collisionless particles. These 'star particles' do not correspond to individual stars, but rather to stellar populations, as resolution typically limits them to thousands or millions of stellar masses. Each star particle thus acts as a simple stellar population (SSP) of a given age and metallicity, populated according to a chosen initial mass function (IMF). Over time, 'stars' within a star particle reach the end of their main sequence lifetimes, and the star particle accordingly loses mass and energy via stellar winds and supernova feedback. The specific implementation of this mass and energy loss varies from simulation to simulation.

Simulating gas is more complicated, because – unlike stars and dark matter – gas behaves as a fluid. Hydrodynamical simulations can be divided into two basic categories depending on their approach to modelling astrophysical fluids: Lagrangian (particle-based) and Eulerian (grid-based).

In the Lagrangian approach, dark matter, stars, and gas are *all* represented by particles. Each particle has a unique ID and carries its own set of properties (mass, velocity, chemistry, etc). Most Lagrangian simulations utilize some variant of Smoothed Particle Hydrodynamics (SPH), in which aggregate properties such as temperature and density are computed by a kernel-weighted sum over some smoothing length. (See Springel, 2010a, for a detailed review of SPH implementation.)

Eulerian, or grid-based, codes divide a volume into cells, then track fluid properties by calculating gradients at the cell boundaries. Most modern cosmological grid codes incorporate adaptive mesh refinement (AMR; Berger & Colella, 1989), which

Simulation	Cosmology	Ω_m	Ω_Λ	Ω_b	h
APOSTLE	*WMAP-7*	0.272	0.728	0.0455	0.704
Auriga	*Planck*	0.307	0.693	0.04825	0.6777

Table 2.1: Cosmological parameters adopted by APOSTLE and Auriga.

automatically adapt the grid's resolution where necessary by subdividing cells that meet specified mass thresholds.

Each approach has its strengths and limitations (for an excellent review, see Somerville & Davé, 2015). Efforts to combine the two have been reasonably successful. The moving-mesh code AREPO, for example, combines Eulerian and Lagrangian approaches by constructing an unstructured mesh that can move with the fluid.

The two simulations analyzed in this work, APOSTLE and Auriga, use Lagrangian and hybrid Eulerian-Lagrangian codes respectively. They are described in the following section.

2.2 Apostle and Auriga

2.2.1 Apostle

Most of the work in this project is based on data from the APOSTLE project (A Project of Simulating The Local Environment; Fattahi et al., 2016b; Sawala et al., 2016). APOSTLE consists of 12 cosmological volumes selected from a ΛCDM N-body cosmological simulation of a 100^3 Mpc^3 periodic box (DOVE; Jenkins, 2013). Volumes were selected to reproduce the kinematic properties of the MW-M31 pair and their surrounding environment out to ~ 3 Mpc, then resimulated at higher resolution with the zoom-in technique described above.

APOSTLE was run using a modified version of the SPH code P-Gadget3 (Springel et al., 2008). P-Gadget3 was originally developed for use in the EAGLE (Evolution and Assembly of GaLaxies and their Environments) project (Schaye et al., 2015; Crain et al., 2015). Its subgrid galaxy formation model includes photoionization due to an X-ray/UV background[1], metal cooling, stellar evolution and supernova feedback, and black-hole accretion and AGN feedback[2].

Star formation is implemented by assuming a metallicity-dependent density thresh-

---

[1] Hydrogen ionization occurs instantaneously at z=11.5.

[2] $<1\%$ of our $z=0$ dwarfs contain black holes that have grown beyond the seed mass.

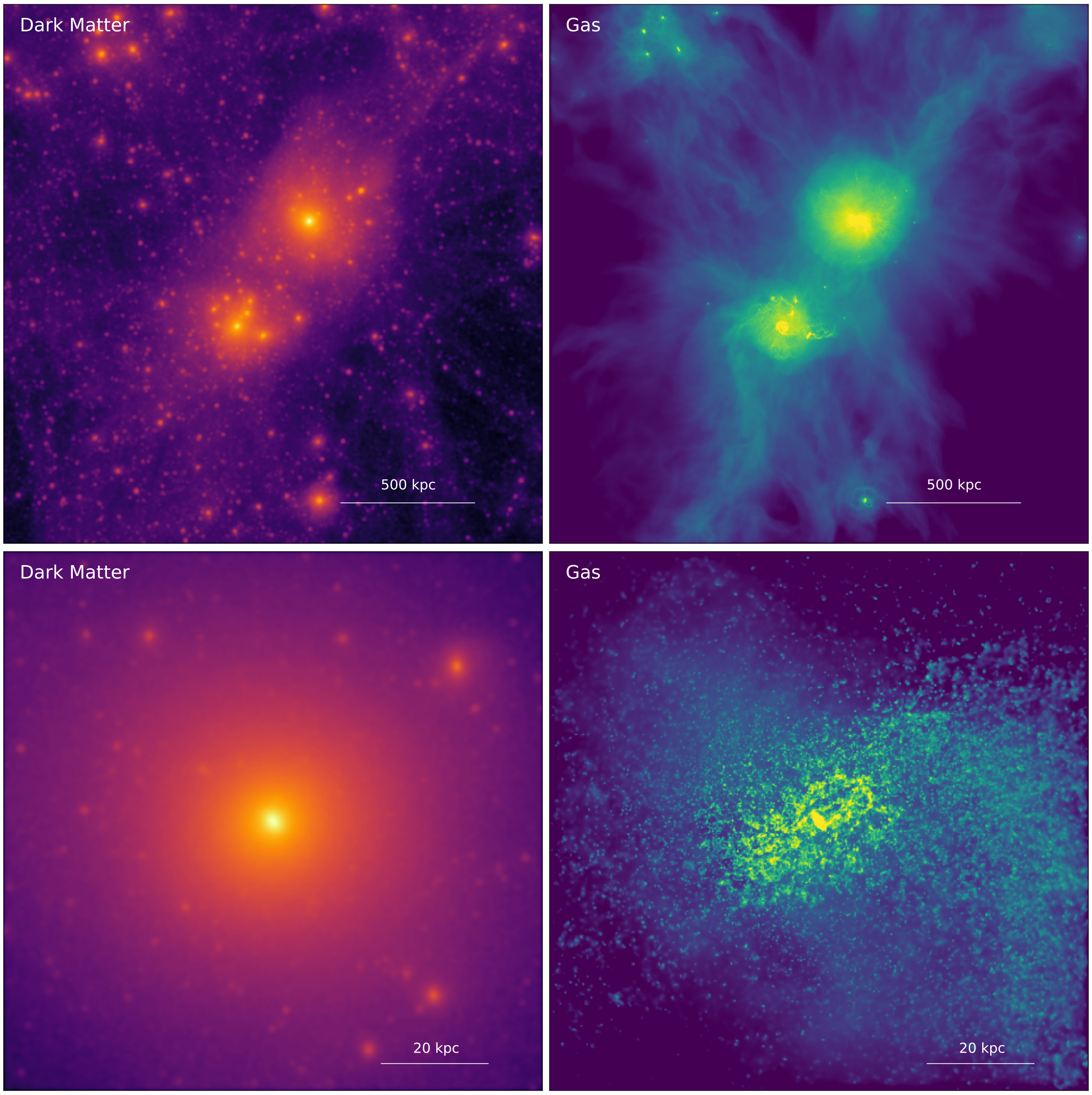

Figure 2.1: Visualizations of Volume 1 of the Apostle simulation, in high resolution. The top panels show a 2 Mpc box centred on the two primary galaxies; the bottom panels show a zoomed-in view of the larger primary (M31 analogue), 100 kpc across. Panels on the left and right correspond to dark matter and gas respectively. Subhalos are clearly visible in the dark matter renders. Many of these subhalos contain the dwarf galaxies we analyze in this work.

old, above which gas particles have a pressure-dependent probability of converting into star particles. Each star particle is populated according to a Chabrier IMF (Chabrier, 2003) in the range $0.1 - 100\ \mathrm{M}_\odot$. At every timestep, the fraction of a star particle's mass that will have evolved off the main sequence is computed, and the corresponding mass and energy are distributed among neighbouring particles. For a complete description of the subgrid physics in EAGLE, see Schaye et al. (2015).

P-Gadget3 was calibrated to approximately match the average size of the stellar component of galaxies and to reproduce the $z = 0.1$ stellar mass function of galaxies down to $M_* \sim 10^8 \mathrm{M}_\odot$. The APOSTLE simulations show that the same subgrid physics can reproduce the stellar mass function of satellites in the Local Group down to $M_* \sim 10^5 \mathrm{M}_\odot$, without further recalibration (Sawala et al., 2016).

Cosmological parameters for APOSTLE were taken from *WMAP-7* (Komatsu et al., 2011), and are summarized in Table 2.1. This differs from EAGLE, which assumed *Planck* cosmology (Planck Collaboration et al., 2014), but the differences should be minimal at Local Group scales.

APOSTLE volumes were simulated at three different numerical resolutions, denoted L1, L2, and L3, with gas particle masses of $\sim 10^4$, 10^5, and $10^6\ \mathrm{M}_\odot$, and gravitational Plummer-equivalent force softening lengths of 134, 307, and 711 pc, respectively. All APOSTLE volumes have been simulated at levels L2 and L3, but to date only five volumes have been run at the highest resolution (L1). Our analysis is restricted to the L1 and L2 realizations of these five volumes (V1, V4, V6, S4, and S5), which we will denote Ap-L1 and Ap-L2. A visualization of one APOSTLE volume is shown in Figure 2.1.

2.2.2 Auriga

Whereas APOSTLE is a suite of SPH simulations emulating the Local Group, Auriga (Grand et al., 2017) consists of ~ 30 isolated Milky Way-sized halos simulated with the moving-mesh code AREPO (Springel, 2010b).

AREPO includes a wide array of physical processes, similar to those in the EAGLE code used for APOSTLE, although it is a magnetohydrodynamic code (incorporating prescriptions for magnetic fields), and reionization occurs later, at $z \sim 6$. As in APOSTLE, Auriga contains prescriptions for AGN feedback, but at $z = 0$ none of Auriga's field dwarfs and $< 1\%$ of its satellites contain black holes.

Star formation in Auriga is implemented by modelling star-forming gas as a two-

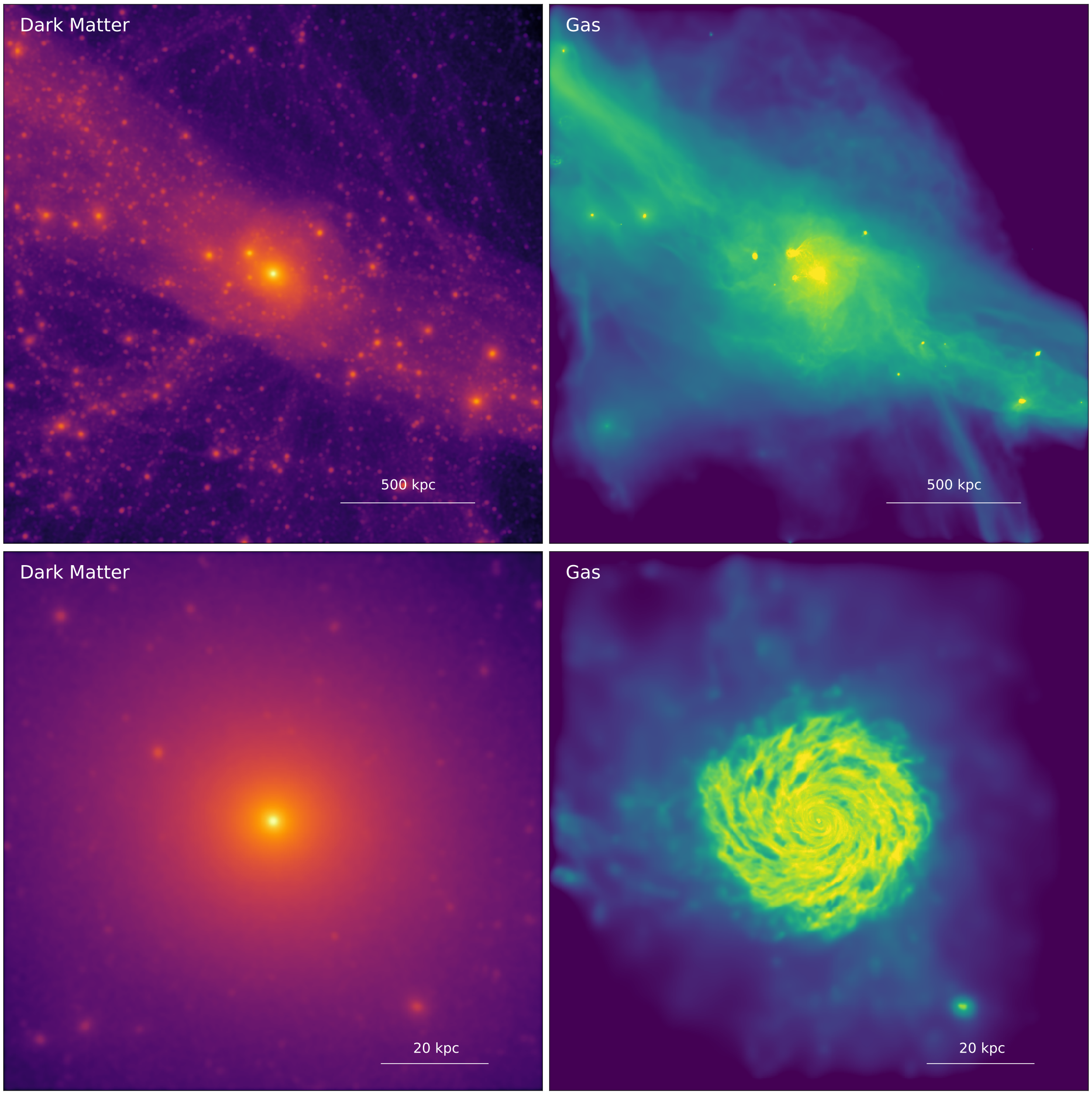

Figure 2.2: Visualizations of Volume 6 of the Auriga simulation, in high resolution. The top panels show a 2 Mpc box centred on the primary (Milky Way analogue) galaxy, and the bottom panels show a zoomed-in view 100 kpc across. Panels on the left and right correspond to dark matter and gas respectively. Subhalos are clearly visible in the dark matter renders. Many of these subhalos contain the dwarf galaxies we analyze in this work.

phase medium. Gas cells are considered to be star-forming if they have densities higher than $n = 0.13cm^{-3}$, at which point they have a probability of forming stars that scales exponentially with elapsed time. As in Apostle, the resulting star particles represent SSPs populated according to a Chabrier IMF, and lose mass and energy over time as stars within the star particle evolve off the main sequence.

Cosmological parameters for Auriga were taken from Planck Collaboration et al. (2014), and are summarized in Table 2.1.

Six Auriga halos have been run at the highest resolution level (L3), which has a typical gas cell mass of $6 \times 10^3 \mathrm{M}_\odot$, roughly a factor of 2 higher resolution than Ap-L1. We restrict our analysis to the Au-L3 and Au-L4 realizations of these 6 halos (halo numbers 6, 16, 21, 23, 24, and 27) and their surroundings. A visualization of one Auriga volume is shown in Figure 2.2.

2.2.3 Simulated Galaxy Sample

Dark matter haloes in Apostle and Auriga are identified using the friends-of-friends (FoF) algorithm (Davis et al., 1985). Bound substructures within each FoF group are then found iteratively using Subfind (Springel et al., 2001; Dolag et al., 2004).

We define galaxies as the baryonic components at the centres of these subhalos. Galaxies' gas masses are defined within R_{200}, and stellar masses within the 'galactic radius' $R_{\rm gal} = 0.15\,R_{200}$[3]. $R_{\rm gal}$ is found to contain essentially all of the stars and star-forming gas in a halo.

Galaxies which inhabit subhaloes other than the main ('central') object in each FoF group do not have a well-defined virial radius. In these cases, we follow Fattahi et al. (2018) and use the average relation between $R_{\rm gal}$ and the maximum circular velocity, $V_{\rm max}$, for central galaxies in APOSTLE to define $R_{\rm gal}$ /kpc$= 0.169(V_{\rm max}/$km s$^{-1})^{1.01}$. The relation between R_{200} and $V_{\rm max}$ is very tight, so using this same definition of $R_{\rm gal}$ for all galaxies (field and satellites) gives equivalent results.

We will refer to the two main galaxies in each Apostle volume as the 'Milky Way and M31 analogues' or, more generally, as the 'primary' galaxies of each volume. In

---

[3] Dark matter halos do not have well-defined edges. A common convention is to describe their sizes using the quantities R_{vir} and M_{vir} or R_{200} and M_{200}. The subscript vir indicates virial quantities: R_{vir} is the radius within which a halo is assumed to be virialized, and M_{vir} is the mass enclosed within that radius. R_{vir} is frequently assumed to be comparable to R_{200}, the radius containing a mass density 200 times the critical density of the universe. This assumption stems from spherical top-hat models of halo formation, which suggest that structures will decouple from the expansion of the universe and collapse into halos when the enclosed density is ~ 178 times the critical density (Peebles, 1993; White, 2001).

Auriga, the main galaxy will be referred to as the ‘Milky Way analogue’ or ‘primary’.

Dwarf galaxies within 300 kpc of a primary are defined as ‘satellites,’ and more distant dwarfs as ‘field’ galaxies, provided they are the central object of their FoF group. We exclude dwarfs beyond 2 Mpc of the APOSTLE primaries’ barycentre, and beyond 800 kpc of the Auriga primaries. This upper limit is to avoid contamination by low-resolution boundary particles, which are found beyond ~ 3 Mpc and ~ 1 Mpc in APOSTLE and Auriga, respectively.

For completeness, we include all simulated galaxies in our analysis, but recommend caution when interpreting those resolved with fewer than 10 star particles. This corresponds to a stellar mass of $\sim 10^5$ $\mathrm{M}_\odot$ in the case of Ap-L1 runs, and $\sim 10^6$ $\mathrm{M}_\odot$ for Ap-L2 runs. We focus on dwarf galaxies in this study, so our sample retains only simulated dwarfs with $M_* < 10^9$ $\mathrm{M}_\odot$.

Chapter 3

Observational Techniques and Analysis

We will compare the SFHs of our simulated dwarf galaxies with available observations of nearby dwarfs. Detailed star formation histories have been derived from HST photometry for ~ 100 dwarf galaxies in and around the Local Group. In this chapter, we introduce the basic process of deriving a SFH from observable quantities, and describe the sample of observations that will be analyzed in this work.

3.1 From CMD to SFH

Inferring a galaxy's lifetime SFH from observations taken at a single snapshot in time is an extremely challenging task. Observers cannot watch their targets evolve, but must use some form of 'galactic archaeology' to infer past evolution from present tracers. Even at a single epoch, parameters such as star formation rate cannot be directly measured, but must be estimated by proxy.

Currently, the 'gold standard' in SFH derivation is the use of resolved colour-magnitude diagrams (CMDs). In principle, a resolved CMD encodes the age of every star in a galaxy, and with sufficiently advanced stellar evolution models it can be reconstructed into a detailed SFH (see Dolphin, 2002; Hidalgo et al., 2011, and references therein).

When a galaxy is too distant to resolve individual stars, SFHs are estimated by using stellar population synthesis (SPS) to interpret integrated spectral energy distributions (SEDs; see review by Conroy, 2013). However, integrated light tends to be dominated by the youngest stars, and the age resolution can be extremely poor at early times. Fortunately, resolved CMDs are available for many dwarf galaxies in the vicinity of the Local Group.

The basic approach to deriving a SFH from a CMD is as follows. First, stellar evolution models are used to generate a suite of simple stellar populations, each of which populates a single CMD isochrone. A linear combination of SSPs is convolved with a noise model, and the resulting CMD compared to an observed one. Weights on the individual SSPs are adjusted to minimize residuals and the final distribution of SSPs converted into a star formation history. This approach is illustrated in Figure 3.1, taken from Weisz et al. (2014).

Despite the many advances in CMD fitting, SFHs derived by modelling photometric observations are still subject to significant uncertainty. These are due in part to observational photometric limitations, but also to the many assumptions required to build a stellar evolution library, including choice of IMF and binary fraction, treatment of blue stragglers, etc., which as yet are poorly understood and difficult to constrain (Gallart et al., 2005). As a result, the choice of stellar evolution library is the single largest systematic in SFHs derived from CMDs, and it is vital that direct comparisons only be drawn between uniformly-reduced galaxies.

Once a stellar evolution library is selected, one of the greatest challenges in CMD fitting is the age-metallicity degeneracy: stars which are old and metal-poor occupy the same region of a CMD as those which are young and metal-rich. This is particularly true on the red giant branch (RGB). This degeneracy can be broken, or at least significantly reduced, if observations are sufficiently deep to resolve the oldest main sequence turnoff (oMSTO; see, e.g., Gallart et al., 2005; Weisz et al., 2011). We will distinguish between 'oMSTO' and 'non-oMSTO' galaxies in our analysis, as there is broad agreement that oMSTO galaxies are the least susceptible to systematic biases. These oMSTO galaxies make up about $\sim 62\%$ of our satellites and 11% of our field dwarf sample.

In this work we take SFHs and their uncertainties directly from the references discussed in the next section (see also Tables A.1 and A.2). Note that many of these SFHs are derived from fields that image only a relatively small region of the galaxy, which, in the presence of strong gradients, may bias the results. We neglect this complication in our comparison with simulations, and assume that the published SFHs are representative of the whole galaxy. We refer the interested reader to Gallart et al. (2005) and Weisz et al. (2014) for a more thorough discussion of these issues.

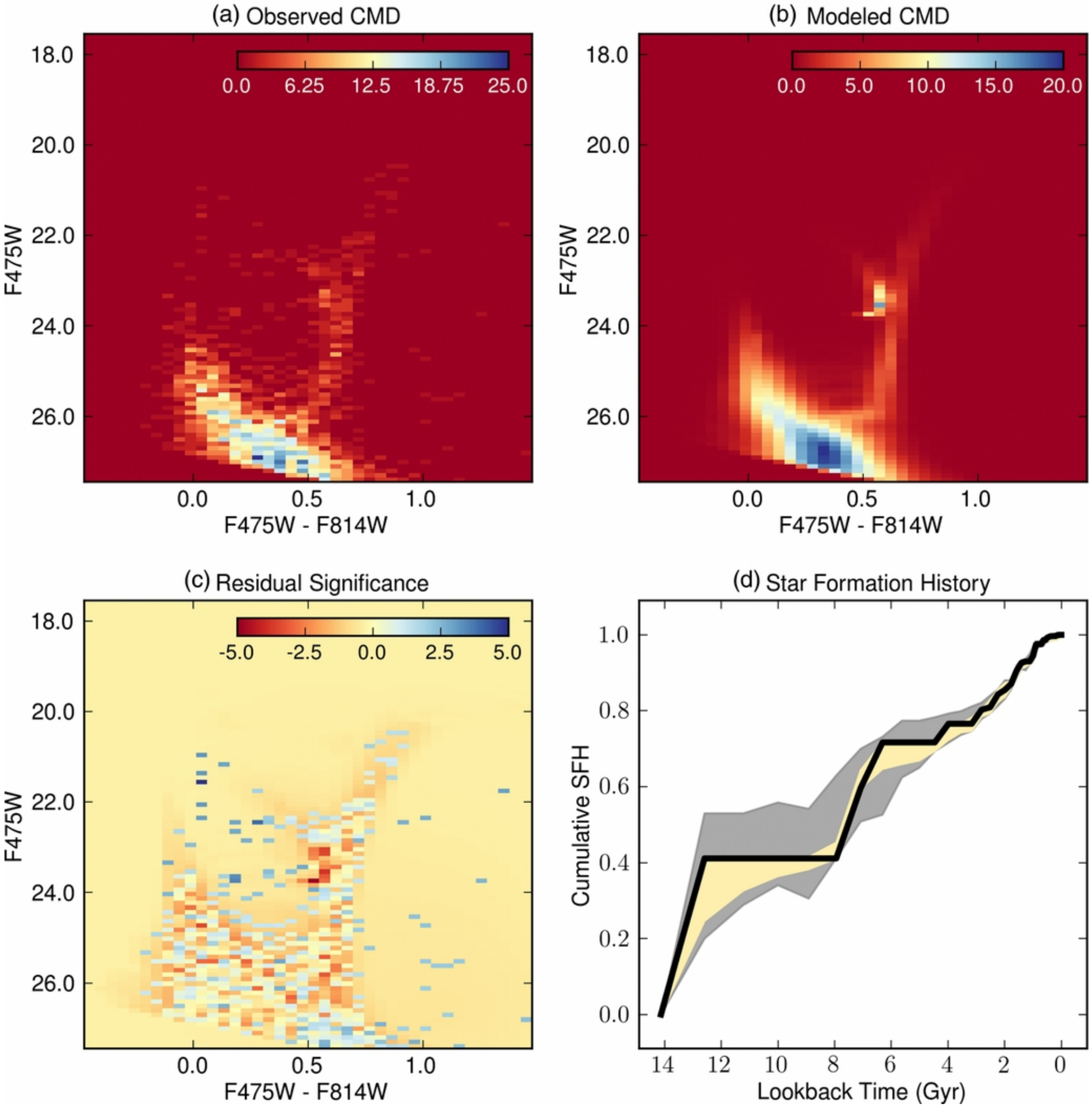

Figure 3.1: The process of deriving a SFH from an observed CMD, in this case of Leo T, taken directly from Weisz et al. (2014). *(a)* The observed CMD, plotted as a Hess diagram (2D density plot). *(b)* A synthetic CMD created by stacking the theoretical CMDs of many individual SSPs. *(c)* The residuals between observed and modelled CMDs. *(d)* The resulting best-fit cumulative SFH, presented as a plot of cumulative mass formed over time. Shaded regions indicate the 1σ confidence interval accounting for random (yellow) and total (random and systematic; grey) uncertainties.

3.2 Observed Galaxy Sample

Our sample of dwarf galaxy observations is taken from the catalogues of Weisz et al. (2011), Weisz et al. (2014), Cole et al. (2014), Gallart et al. (2015), and Skillman et al. (2017). These five sources provide SFHs derived from HST multi-band imaging, reduced and analysed with similar methodology, for a total of 101 galaxies with stellar masses in the range $6.5 \times 10^3 < M_* / \mathrm{M}_\odot < 3.4 \times 10^9$. Of these 101 galaxies, 72 are classified as field dwarfs and 29 of as satellites of either the MW or M31. This classification is based on the same simple distance cut used for the simulations, i.e., those within 300 kpc of a primary are defined as satellites and those beyond as field dwarfs.

Distances and stellar masses are taken from the Updated Nearby Galaxy Catalogue (Karachentsev et al., 2013), assuming, for simplicity, a uniform B-band mass-to-light ratio of 1 in solar units. Tables A.1 and A.2 list the galaxies selected from these compilations, together with the derived data we use in this analysis. The sample includes examples of a wide range of morphological types, including dSphs, dIrrs, and dTs, as well as the rare dwarf elliptical M32 (Monachesi et al., 2012). Not included are the Small and Large Magellanic Clouds, as their large size makes them unsuitable for study with HST's small field of view (Weisz et al., 2014).

The observed sample extends to stellar masses a bit below the $\sim 10^5$ $\mathrm{M}_\odot$ minimum mass we can resolve in the simulations. It also includes a few galaxies with $M_* > 10^9$ $\mathrm{M}_\odot$. However, only 10 galaxies in total are beyond the stellar mass limits of the simulated sample, so this slight mismatch is unlikely to impact the conclusions of our comparison.

The galaxies in this sample are not strictly restricted to those within the Local Group. Indeed, the entire compilation of Weisz et al. (2011) consists of dwarfs beyond the zero velocity surface of the Local Group, out to a maximum distance of ~ 4.6 Mpc from the Milky Way. However, for brevity we will frequently refer to this population as 'Local Group observations.'

Chapter 4

The SFHs of Local Group Dwarf Galaxies

This chapter presents the star formation histories of the simulated and observed dwarf galaxy samples introduced in Sections 2.2 and 3.2.

4.1 Defining SFHs

There are two basic ways to represent a star formation history: cumulatively, which measures total stellar mass as a function of time, and differentially, which measures the stellar mass formed in discrete time intervals. The latter is equivalent to an average measure of the star formation rate as a function of time.

Cumulative SFHs are commonly used in the literature, as they are the most robustly constrained by observational data. However, constraining curves to start at 0 and end at 1 minimizes the appearance of temporal variation in SFR. On the other hand, differential SFHs are excellent for showing temporal variation, but they are subject to binning effects. In this work, we utilize both cumulative and differential representations of dwarf galaxy star formation histories, depending on the application.

When working solely with simulated data, we parametrize SFHs by computing the fraction of stars formed in three intervals of cosmic time, t: $f_{\rm old} \equiv f_{\rm o}$ refers to 'old' stars ($t_{\rm form} < 4$ Gyr), $f_{\rm int} \equiv f_{\rm i}$ to 'intermediate-age' stars ($4 < t_{\rm form}/{\rm Gyr} < 8$), and $f_{\rm young} \equiv f_{\rm y}$ to 'young' stars ($t_{\rm form} > 8$ Gyr). We then express these fractions as SFRs normalized to the past average, $\bar{f} = M_* / t_0$, where $t_0 = 13.7$ Gyr is the age of the Universe, and M_* is the stellar mass of a dwarf at $z = 0$ (Benítez-Llambay et al., 2015). In other words,

$$f_j = \frac{1}{X} \frac{\Delta M_j / \Delta t_j}{\bar{f}}, \tag{4.1}$$

where the subscript j stands for either the 'old', 'intermediate', or 'young' component, and

$$X = \frac{1}{\bar{f}} \sum_{j} \frac{\Delta M_j}{\Delta t_j} \tag{4.2}$$

is a normalizing coefficient that ensures that $f_\mathrm{o} + f_\mathrm{i} + f_\mathrm{y} = 1$. With this definition, galaxies that form stars at a constant rate will have $f_\mathrm{o} = f_\mathrm{i} = f_\mathrm{y} = 1/3$.

When incorporating observational data into our analysis, we use cumulative measures to describe the SFH, including f_XGy (the fraction of stars formed in the first X Gyrs of evolution) and τ_X (the cosmic time by which the first $X\%$ of stars were formed).

In this work, 'time' will refer exclusively to cosmic time. A time of $t = 0$ corresponds to the beginning of the universe, and $t = 13.7$ Gyr corresponds to present day ($z = 0$).

4.2 SFHs in Apostle and Auriga

We begin our analysis with the star formation histories of simulated dwarfs from APOSTLE and Auriga. As outlined in Section 4.1, we use the fractions f_o, f_i, and f_y here to emphasize changes in SFR across cosmic time.

These SFHs are presented in Figure 4.1. The top row of panels plots the individual SFHs of all Ap-L1 galaxies. These are displayed using ternary plots, a type of triple-axis plot that provides a concise visualization of data whose points are composed of three quantities that add to unity (as is the case for f_o, f_i, and f_y). Labels in the figure, and details in the caption, explain how to read these plots. The three top panels correspond to three bins in stellar mass, and point styles indicate environment: field dwarfs are plotted as blue diamonds, and satellites as green circles.

The first feature to notice from these ternary plots is the remarkable diversity of SFHs, even between galaxies of similar mass and environment. The second point of note is that, despite sizeable galaxy-to-galaxy scatter, there are clear mean trends with both stellar mass and environment. This is more easily appreciated in the middle and bottom rows of Figure 4.1, which show the median SFHs of field and satellite dwarfs respectively. The mean SFHs of Ap-L1 galaxies are shown in histogram form, with shaded regions spanning the $16^\mathrm{th} - 84^\mathrm{th}$ percentiles. Coloured points show the median SFHs of Ap-L2, Au-L3, and Au-L4 galaxies.

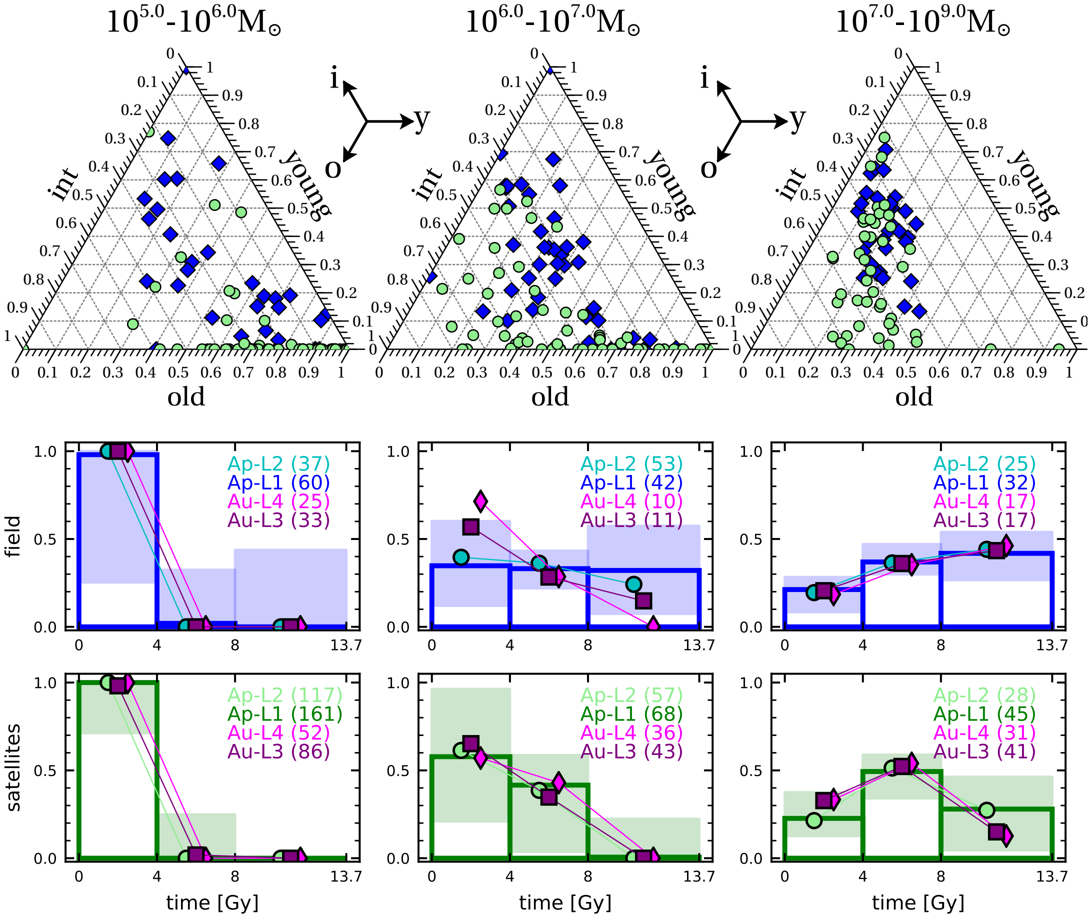

Figure 4.1: The star formation histories (SFHs) of Apostle and Auriga dwarfs. *Top row:* Ternary plots showing the SFHs of Ap-L1 galaxies in three bins of stellar mass, as indicated by the top legend. The arrows indicate how to read the old (f_o; down and left), intermediate (f_i; up and left), and young (f_y; horizontally right) SFH fractions for each galaxy. Different symbols indicate environment: field and satellite are indicated by blue diamonds and green circles respectively. *Middle row:* The median values of f_o, f_i, and f_y for field galaxies in each mass bin. Ap-L1 results are shown in bar form, with shaded regions spanning the 16th to 84th percentiles. Ap-L2 results are shown by cyan circles, Au-L3 by purple squares, and Au-L4 by magenta diamonds. For clarity, the Ap-L2 and Au-L3 markers have been offset slightly. The number of galaxies in each mass bin is given in parentheses. *Bottom row:* As middle row, but for satellites. Note the systematic trend with stellar mass of the average simulated SFHs, and that said trends are robust to changes in the mass and spatial resolution of the simulations. In each mass bin, the satellite SFHs are similar to those of the isolated field galaxies, except for a significant reduction in the young stellar population.

Looking first at the field dwarfs, it is clear that the smallest dwarfs form most or all of their stars in the first ~ 4 Gyr of the universe (i.e, on average have $f_o \sim 1$). Moving to higher stellar mass increases the relative fraction of young stars, such that intermediate-mass galaxies have roughly constant star formation histories, and the most massive dwarfs have steadily increasing star formation rates.

The satellites show a similar trend with mass, except for a sharp suppression in star formation at recent times. This suppression is inversely proportional to stellar mass, with the largest satellites impacted least. In other words, field and satellite dwarfs have very similar evolution until relatively late times, when satellites lose the ability to continue star formation.

These results are in remarkably good agreement across our four simulation suites (medium- and high-resolution runs of each Apostle and Auriga). This agreement is similarly apparent in Figure 4.2, which directly plots the mass dependence of each f_o, f_i, and f_y for field and satellite dwarfs.

Given the differences in hydrodynamical treatment between Apostle and Auriga, and the order-of-magnitude differences between the high- and medium-resolution runs of each, this agreement is reassuring. It suggests that the results of Figure 4.1 are a robust prediction for low-mass halos in ΛCDM, and not simply an artifact of numerical resolution or subgrid physics implementation.

For clarity and ease of presentation, the remainder of this analysis will show results from Ap-L1 only. The corresponding figures for Au-L3 data can be found in Appendix A.2.

4.3 Comparison with Local Group Dwarfs

Our cosmological simulations predict clear trends: in the field, low-mass galaxies form all of their stars at early times, and increasing stellar mass leads to an increasingly important population of intermediate and late-time star formation. Satellite evolution mirrors that of field dwarfs at early and intermediate times, but with suppressed star formation at recent epochs. Do observations of real galaxies in the vicinity of the Local Group show the same trends?

Because cumulative measures of SFHs are much more robustly constrained for observational data than differential measures are, we cannot directly compare f_o, f_i, and f_y in the simulations and observations. Instead, we will express SFHs in terms of the cumulative fractions f_{4Gy} (the fraction of stars formed in the first 4 Gyr, equal

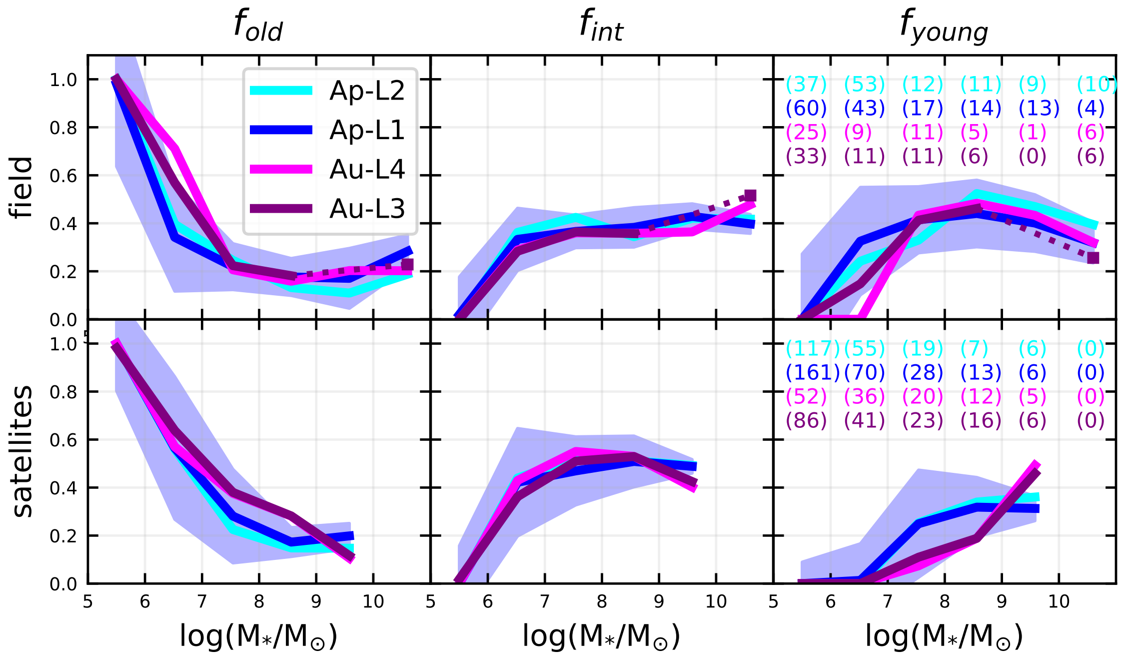

Figure 4.2: Median f_o, f_i, and f_y as a function of M_* for Ap-L1 and Au-L3 (high-res), and Ap-L2 and Au-L4 (medium-res) galaxies. Shaded regions show 1σ dispersion for Ap-L1 data. *Top.* Centrals (field dwarfs and primary galaxies). *Bottom.* Satellites. Numbers in parentheses indicate the number of galaxies in each mass bin. Note that the results for Auriga and APOSTLE are nearly identical, despite the fact that the two simulation suites use different hydrodynamical codes and independent star formation and feedback algorithms.

to f_o) and $f_{8\mathrm{Gy}}$ (equivalent to the combined f_o and f_i).

The mass dependence of these fractions is shown in Figure 4.3, with the left and right hand columns corresponding to field and satellite dwarfs respectively. APOSTLE data is shown in blue (field) and green (satellites); Local Group observations are plotted in red.

Galaxies with sufficiently deep photometry to resolve the oMSTO are indicated with heavy red points, and they appear to follow qualitatively similar trends to those seen in the simulations. More massive field galaxies have lower values of $f_{4\mathrm{Gy}}$ and $f_{8\mathrm{Gy}}$ than low-mass systems do, indicating extended star formation activity that continues, in some cases, to the present day. (Simulated galaxies with non-zero star formation at $z = 0$ are indicated with a central 'dot' in the figure.) Satellites show a similar trend with stellar mass, albeit with reduced recent star formation, which translates into systematically higher values of $f_{4\mathrm{Gy}}$ and $f_{8\mathrm{Gy}}$ than those of field dwarfs.

The agreement between observations and simulations breaks down when we consider galaxies with photometry too shallow to resolve the oMSTO, indicated in the figure by translucent red points. This population dominates the field dwarfs (64 out of 72 field dwarfs are non-oMSTO systems), and appears to have much higher values of $f_{4\mathrm{Gy}}$ and $f_{8\mathrm{Gy}}$ than seen in the simulations. This would imply a large population of dwarfs that grows much more quickly at early times than simulated dwarfs do. There is also no apparent mass trend in these dwarfs, in contrast to the strong mass trend found in the simulations.

Before taking this discrepancy too seriously, it is important to note the very large uncertainties that apply to non-oMSTO systems (error bars indicate the 16^{th} and 84^{th} percentiles, and include the quoted systematic and statistical errors). However, these error bars may not be enough to reconcile simulated and observed SFH trends unless there is some other, unaccounted-for systematic influencing the results.

Interestingly, many of the non-oMSTO dwarfs do not appear to form *any* stars at intermediate times. This is shown more clearly in Figure 4.4, which plots the difference $f_{8\mathrm{Gy}} - f_{4\mathrm{Gy}}$ for simulated and observed dwarfs. In the simulations, the only dwarfs with $f_{8\mathrm{Gy}} - f_{4\mathrm{Gy}} \sim 0$ are those with $f_o \sim 1$, i.e., those which form all of their stars in the first 4 Gyrs and do not resume star formation.

Either there is some physical mechanism not captured in the simulations that can halt star formation for several Gyrs and then resume it again, regardless of a

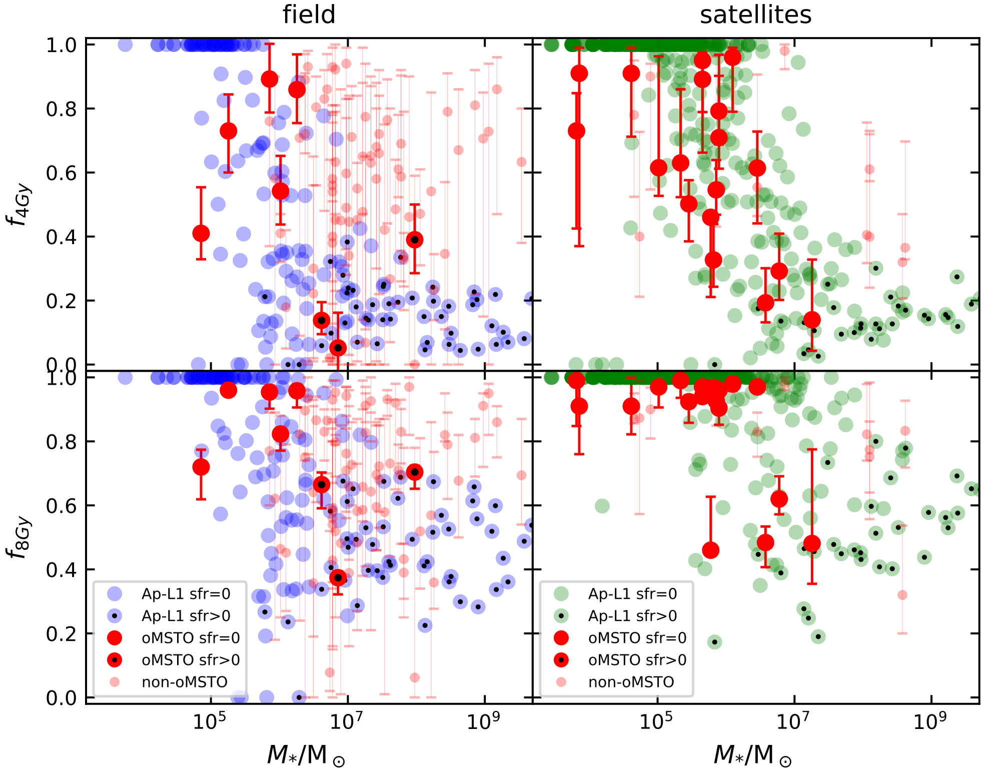

Figure 4.3: The fraction of stars formed in the first 4 ($f_{4\mathrm{Gy}}$) and 8 ($f_{8\mathrm{Gy}}$) Gyr of cosmic evolution, as a function of stellar mass. Apostle galaxies are shown in blue (field dwarfs) and green (satellites); observed galaxies are in red. Error bars in the latter indicate the 16th and 84th percentile bounds on the combined statistical and systematic uncertainties, as given in the literature. SFHs published in Gallart et al. (2015), which make up 6 of the 8 oMSTO field dwarfs, do not quote systematic uncertainties. We assign them the median error of the other oMSTO galaxies (see Tables A.1 and A.2). Filled red circles highlight observed galaxies where the photometry reaches the oldest main sequence turnoff, and a central black 'dot' indicates the oMSTO dIrrs Aquarius, IC1613, and LeoA, which are still forming stars at the present day.

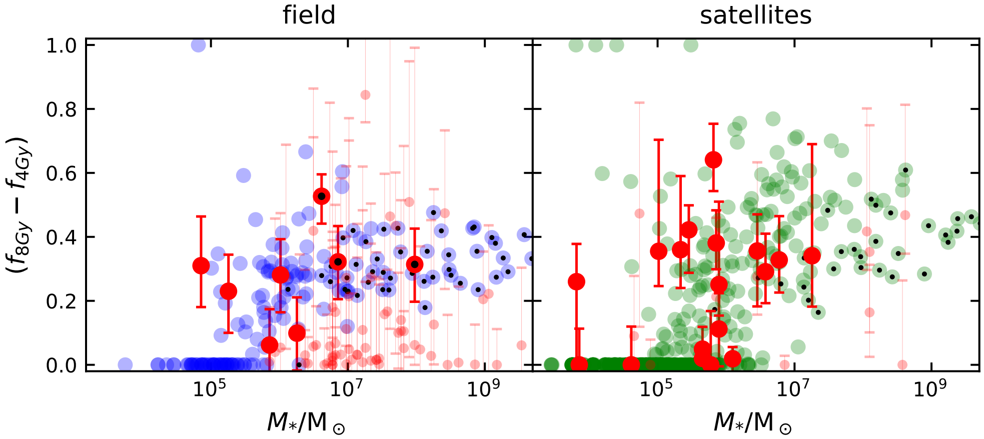

Figure 4.4: As Fig. 4.3, but for the difference between the fraction of stars formed by the first 4 and 8 Gyrs of cosmic evolution. Note the large number of non-oMSTO observed galaxies (open red symbols) that appear to form no stars in that time period.

galaxy's stellar mass[1], or there is a systematic effect in the SFH modelling that favours assigning old ages (i.e., $t_{\mathrm{form}} < 4$ Gyr) to the majority of stars formed before $t = 8$ Gyr. As the discrepant population of $f_{\mathrm{8Gy}} - f_{\mathrm{4Gy}} \sim 0$ dwarfs occurs only in the non-oMSTO dwarfs, which are known to be more prone to systematic uncertainties (see, e.g., Gallart et al., 2005; Weisz et al., 2011), we will proceed on the assumption that non-oMSTO data is unable to robustly constrain SFHs at early and intermediate times.

In other words, for data that are sufficiently deep to constrain early and intermediate epochs of star formation, the observations and simulations are in fairly good agreement. The remainder of this analysis will therefore be restricted to the oMSTO galaxies.

4.4 The Earliest and Latest Stages of Star Formation

Having established that simulated and observed dwarfs evolve similarly, we can analyze them together to look for additional trends in their SFHs. In the following sections we explore the earliest and latest stages of star formation.

4.4.1 Early Star Formation

Dwarfs of all masses and in all environments have clearly formed significant populations of stars at early times (in this analysis, all dwarfs have non-zero values of f_{4Gy}; this is consistent with other observations (Benítez-Llambay et al., 2015; Gallart et al., 2015)). But how early does star formation start? Does the onset of star formation depend on stellar mass? These questions are addressed in Figure 4.5, which plots f_{1Gy}, the fraction of stars formed in the first 1 Gyr, as a function of stellar mass. This is the earliest time constrained by observed SFHs, and corresponds to a stellar age of ~ 12.6 Gyr.

At all masses, the majority of simulated dwarfs have very small values of f_{1Gy}. This is true in all environments: $\sim 70\%$ of field dwarfs and $\sim 50\%$ of satellites formed fewer than 5% of their stars in the first ~ 1 Gyr. Observed oMSTO dwarfs, while consistent with the trend to higher f_{1Gy} at low masses exhibited by some APOSTLE galaxies, lack the $f_{\mathrm{1Gy}} \sim 0$ population that dominates the simulations.

---

[1] Cosmic reionization has been invoked to explain galaxies that may have a prolonged gap in star formation activity (Benítez-Llambay et al., 2015; Ledinauskas & Zubovas, 2018), but this argument is only plausible for the lowest-mass galaxies.

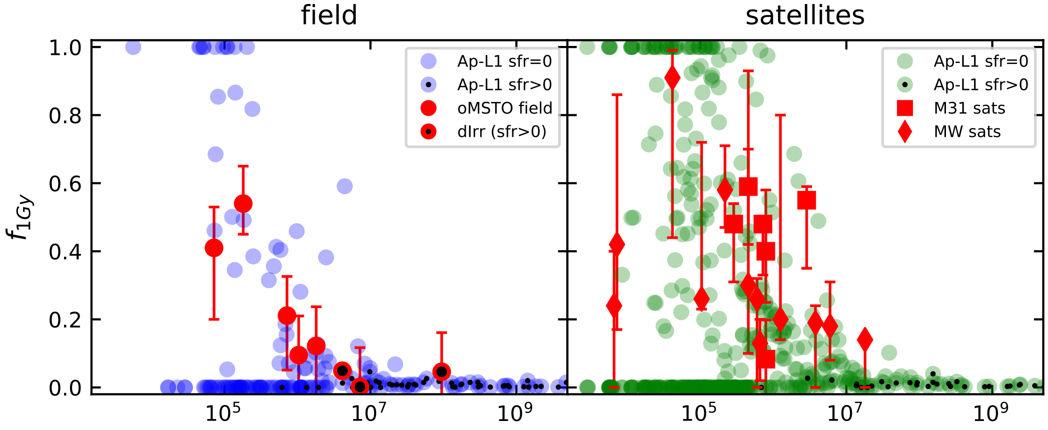

Figure 4.5: The cumulative fraction of stars formed in the first ∼ 1 Gy of cosmic evolution, for APOSTLE and oMSTO galaxies only. Error bars indicate the 16th and 84th percentile bounds on the combined statistical and systematic uncertainties, as published in the literature. Symbols differentiate observed field dwarfs (circles) from satellites of M31 (squares) and of the Milky Way (diamonds). Black dots indicate the dIrrs Aquarius, IC1613, and LeoA, which are still forming stars at the present day.

Before reading too much into this apparent discrepancy, the simulations' limitations must be considered. Simulations are sensitive not only to resolution effects, but to choices in subgrid implementation such as APOSTLE's input threshold for star formation, neglect of molecular cooling, and absence of a cold gaseous phase.

APOSTLE's implementation of cosmic reionization, which occurs instantaneously at $z = 11.5$ ($t \sim 0.4$ Gyr), may also contribute to these results. Recent observations suggest a somewhat later redshift for reionization, perhaps as low as $z_{\rm reion} \sim 5.3$ ($t \sim 1.2$ Gyr; Glazer et al., 2018; Planck Collaboration et al., 2018). It is therefore possible that the adoption of an early reionization redshift could have unduly reduced the fraction of stars formed in the first ~ 1 Gyr. Indeed, field galaxies in Au-L3, which sets $z_{\rm reion} = 6$, also lack the low-mass/low-$f_{\rm 1Gy}$ population and are more closely matched by observations (see Fig. A.3). On the other hand, Au-L3 satellites match observations less well; see Appendix A.2 for further discussion.

Although most APOSTLE dwarfs formed few, if any, stars in the first ~ 1 Gyr, star formation does begin shortly thereafter. 90% of all Ap-L1 dwarfs with > 10 star particles had begun forming stars by $t \sim 1.8$ Gyr. This value depends heavily on mass and resolution: splitting the simulated sample in the same three mass bins as in Fig. 4.1 (10^5-10^6; 10^6-10^7; 10^7-10^9, in units of $M_\odot$) we find that 90% of APOSTLE dwarfs have, respectively, first-star formation times earlier than $t_i = 1.2$, 0.8 and 0.4 Gyr for Ap-L1 runs, and $t_i = 1.9$, 0.9 and 0.5 Gyr for Ap-L2 runs. This mass/resolution dependence indicates that our estimates of $f_{\rm 1Gy}$ have not converged, and could easily rise in higher resolution simulations, or in simulations with a later epoch of reionization.

With the caveat that our precise estimates of $f_{\rm 1Gy}$ are not converged, it does appear that essentially all simulated dwarfs do have significant old populations, qualitatively consistent with observations. A more meaningful comparison would require simulations of much higher resolution, with improved physical treatment of the formation of the first stars.

4.4.2 Late Star Formation

There has been a great deal of recent interest in the physics of 'quenching,' or the extinction of star formation. This is frequently parametrized by the value τ_{90}, the time at which a galaxy had formed 90% of its total stellar mass. Figure 4.6 examines the dependence of τ_{90} on stellar mass and proximity to the nearest primary galaxy.

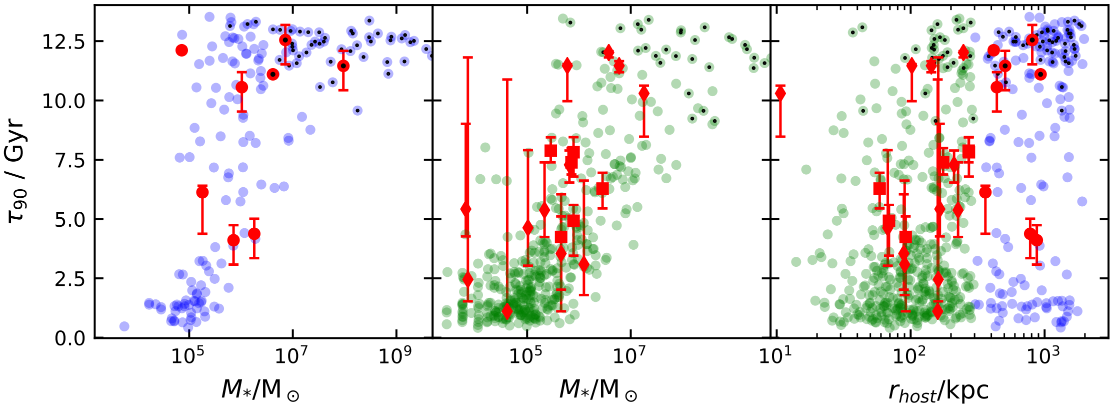

Figure 4.6: The cosmic time at which galaxies have formed 90% of their stars, τ_{90}, as a function of stellar mass (left and middle panels, showing field and satellite dwarfs, respectively) and as a function of distance from the nearest primary (right-hand panel). Values of τ_{90} are interpolated from the published SFHs. Error bars show the corresponding width of the 16th-84th percentile error envelope given in the literature. As in Figs. 4.3-4.5, galaxies taken from Gallart et al. (2015) are assigned the median error bars of all other oMSTO galaxies. Symbols differentiate observed field dwarfs (circles) from satellites of M31 (squares) and of the Milky Way (diamonds). Black central dots indicate the dIrrs, which are still forming stars today.

There is excellent agreement between the τ_{90}'s of simulated and observed dwarfs. Both exhibit clear mass trends, particularly in the satellite populations, for which star formation ended very early at low masses and continues to the present day at high masses. Galaxies marked with a central 'dot' in Fig. 4.6 are still forming stars at $z = 0$. In the simulations, these are overwhelmingly massive galaxies, usually with $M_* > 10^7$ M$_\odot$, in qualitative agreement with the satellites of the MW and M31, where only the most massive (e.g., the Magellanic Clouds, or M33, not included in our sample) are still forming stars today.

Note that if this trend were to hold at lower stellar masses it would also be consistent with the results of Brown et al. (2014), who report that six ultra-faint dwarfs (with masses below the lower mass limit of the samples used in this work) are consistent with having finished forming stars by $t \sim 2$ Gyr.

Simulated field dwarfs (left-hand panel in Fig. 4.6) tend to fall into one of two categories: those that form stars until late times (or are still forming them at $z = 0$, identified with a central 'dot' in the figure), and those where star formation shuts off early on, with few examples in between. There are too few oMSTO field dwarfs for a detailed comparison, but there are no obvious deviations from this trend in the observed τ_{90}. The apparent dichotomy in τ_{90} is not seen in the satellite population, where there are many systems with intermediate values of $\tau_{90} \sim 7$ Gyr.

Finally, the right-hand panel of Fig. 4.6 shows the dependence of τ_{90} on distance to the nearest primary galaxy. No obvious correlation may be discerned from this plot, either in observed dwarfs or in simulated ones.

These trends in τ_{90} are consistent with previous studies on dwarf galaxy quiescence (e.g. Davies et al., 2019; Fillingham et al., 2016, 2018; Simpson et al., 2018), which find similar dependence on mass and environment. These authors suggest that low-mass satellites may have had their star formation extinguished by the effects of ram-pressure and tidal stripping during their orbital evolution within in their host halos.

4.5 Summary: the SFHs of Local Group Dwarfs

The star formation histories we have measured from the Apostle and Auriga simulations, and those derived from Local Group observations with sufficient photometric depth to constrain the earliest periods of star formation, are remarkably consistent and can be neatly summarized by a few observations. First, in isolated field dwarfs, star formation histories vary with final stellar mass: low-mass dwarfs form stars only for the first few Gyr of their lives, whereas their more massive counterparts have extended star formation histories. Second, satellite dwarfs have similar evolution at early and intermediate times, but their late-time star formation is suppressed by accretion into their hosts' halos.

These results are consistent with the recent findings of Garrison-Kimmel et al. (2019), who investigated the impacts of mass and environment on the star formation histories of dwarfs in the FIRE-2 simulations (Hopkins et al., 2014). The Feedback In Realistic Environments (FIRE; Hopkins et al., 2014) project uses cosmological zoom-in simulations to study feedback and galaxy evolution; FIRE-2 introduced updated numerical methods.

Garrison-Kimmel et al. (2019) analyzed dwarf galaxies from a suite of zoom-in simulations targeting five different environments: truly isolated field dwarfs, centrals and satellites around isolated Milky Way analogues, and centrals and satellites around Local Group analogues. The latter two environments are equivalent to our study of the Auriga and APOSTLE simulations, respectively.

They found qualitatively similar results to ours: low-mass galaxies form early, large galaxies have extended star formation histories, and the presence of primaries serves to suppress late-time star formation. Interestingly, they find little difference between satellites and centrals around Local Group analogues, whereas – especially for dwarfs with $M_* \ (z = 0) = 10^{6-7}\mathrm{M}_\odot$– APOSTLE shows systematic differences. However, our two sets of findings are consistent within the errors. The differences are unlikely to be explained by the field dwarfs' average proximity to their hosts, as they choose the same selection as we did: satellites are defined by $d_{host} < 300$ kpc, and field by $300\,\mathrm{kpc} < \mathrm{d_{host}} < 2\,\mathrm{Mpc}$.

Garrison-Kimmel et al. (2019) also highlighted differences between the evolution of field dwarfs in their three environments: those around Local Group analogues tended to form earlier than those around Milky Way analogues, and the highly isolated dwarfs had yet more extended star formation histories. We cannot directly comment on the last case, lacking our own sample of truly isolated dwarfs, but it does seem plausible given our observations on the impact of environment. However, we do not see an equivalent offset between Auriga and APOSTLE field dwarfs. Indeed, the only offset we see is for dwarfs with $M_* \ (z = 0) = 10^{6-7}\mathrm{M}_\odot$ (the mass range where they see the largest discrepancy), and we find the *opposite* trend, with Auriga (Milky Way) centrals forming earlier on average than APOSTLE (Local Group) centrals.

The origins of these discrepancies are unclear, but may well be an outcome of the remarkable diversity of dwarf star formation histories. All of the results presented in Garrison-Kimmel et al. (2019) are within the 68^{th} percentile range of our own.

Chapter 5

The Origins of SFH Trends in Simulated Field Dwarfs

In Chapter 4, we found clear and systematic trends between stellar mass and average SFHs. This chapter presents a preliminary exploration of the origin of these trends.

To study the evolution of our galaxies in greater detail, we tracked the medium resolution (L2) Apostle field dwarfs backwards through the simulation as far as $t = 1\text{Gyr}$. The technical details of this tracking are detailed in Section 5.1. Our analysis of this evolutionary data is presented in Section 5.2.

The aim of this chapter is to understand how the evolution of an isolated dwarf galaxy depends on its stellar mass (or, perhaps, on other quantities which also correlate with stellar mass). As satellite galaxies are futher influenced by environmental interactions, which are challenging to disentangle from intrinsic mass-related effects, we limit our analysis here to the study of field dwarfs.

5.1 Galaxy Tracking

As described in Section 2.2.3, dark matter halos in Apostle are found using the algorithm friends-of-friends (FoF), and bound substructures within each FoF group are identified with the halo finder Subfind. Every subhalo can thus be identified by the combination of its group (FoF, halo) and subgroup (Subfind, subhalo) numbers. Halos and subhalos are ordered by mass: the largest subhalo (i.e. the M31 analogue) is group 1, subgroup 0; its largest satellite is group 1, subgroup 1. Subgroup numbering is halo-specific, so the largest subgroup in every group is number 0.

Simulation output is saved in snapshots, equally spaced in log t (time). Data is saved in 3 file types: *group*, *particle data,* and *snapshot*. Group files contain the global properties (total mass, total star formation rate, centre of potential, etc.) of every group and subgroup. Particle data files contain the properties of every particle that is assigned to an FoF group, and snapshot files list the properties of every single particle in the simulation. This work utilized only the first two file types.

We tracked all medium-resolution APOSTLE field galaxies with $z = 0$ stellar masses $M_* > 10^5 \mathrm{M}_\odot$ back through time as far as $t = 1$ Gyr. Tracking galaxies is a two-stage process: first, we identify each galaxy's group and subgroup numbers as a function of time, and then we separately calculate galactic properties in each snapshot. Separating the process into two independent stages allows for the comparison of different methods for calculating galactic properties at reduced computational expense.

5.1.1 Subhalo Identification through Time

Subhalos were linked between successive snapshots by tracking their most-bound dark matter particles backwards through time. Tracking was initiated by providing a list of target halos, identified by their halo/subhalo number combinations. The dark matter particles corresponding to each halo were identified and sorted by binding energy. Finally, the particle IDs of the most tightly bound 10% were passed to the next stage.

At each snapshot after the first, the tracking process was implemented as follows. A list of particle IDs (the most tightly bound dark matter particles from the preceding snapshot) was provided as input. The algorithm determined the halo/subhalo combination to which the majority of these particles belonged, then identified all of the dark matter particles belonging to that subhalo. These particles were sorted by binding energy, and the IDs of the 10% most bound were passed to the next snapshot. This process iterated until a time of $t = 1$ Gyr had been reached.

Tracking was made significantly more efficient by using the particle data files, which only contain particles assigned to an FoF group, rather than the snapshot files which include all particles in the simulation. However, this introduced a significant limitation in how far back galaxies could be tracked. Dwarf galaxies, small even at $z = 0$, frequently become too small to be identified as substructures by FoF. When this occurs, the particles are no longer written to file, and the galaxies cannot be tracked further.

5.1.2 Galaxy Properties through Time

Given a 'roadmap' listing each galaxy's halo and subhalo number as a function of snapshot, determining the evolution of galactic properties should have been very straightforward. Two basic approaches exist: using the subhalo properties recorded in the group files by Subfind, or using the particle data files to calculate these values by hand.

Upon implementing the first approach, it rapidly became evident that further refinement would be required. Subfind's halo-finding algorithm is prone to mis-assigning particles when small bodies pass near each other, leading to erratic spikes and valleys in halo/galaxy mass. This issue, and our attempts at circumventing it, are described below.

Subtleties: Subfind Assignment

Tracking a core of dark matter particles back through time gives us a string of halo progenitors, which ideally would correspond to a single physical object evolving with time. However, the subgroup identified by Subfind in each snapshot does not always correspond to the physical subhalo we are trying to track. Particles assigned to one subhalo in one snapshot may be assigned to another in the next, depending on how Subfind decomposes a region into substructures. This is typically only an issue when two objects pass near to each other, but as subhalos grow through mergers, close encounters are reasonably frequent.

Consider first the case in which a subhalo we are tracking encounters a similarly-sized clump. An example of this is illustrated in Figure 5.1. Our subhalo is initially the largest object of its group, with subhalo number $s_i = 0$. As the clump approaches, Subfind groups it together with our subhalo into one large, extended, transient structure. However, if Subfind determines that the clump should be $s = 0$, then the extended edges of our subhalo are assigned temporarily to the clump and the core dark matter particles belong to a much smaller subhalo with $s_i = 1$. Our recorded subhalo mass thus dips dramatically until the subhalo and clump separate again, or merge completely. (Note that, since we track backwards through time, we would actually see this process occur in reverse.)

Alternatively, if our subhalo encounters a significantly smaller clump, it will remain the central object ($s_i = 0$) but will temporarily include both its own particles and those belonging to the clump. The result is a dramatic spike in mass.

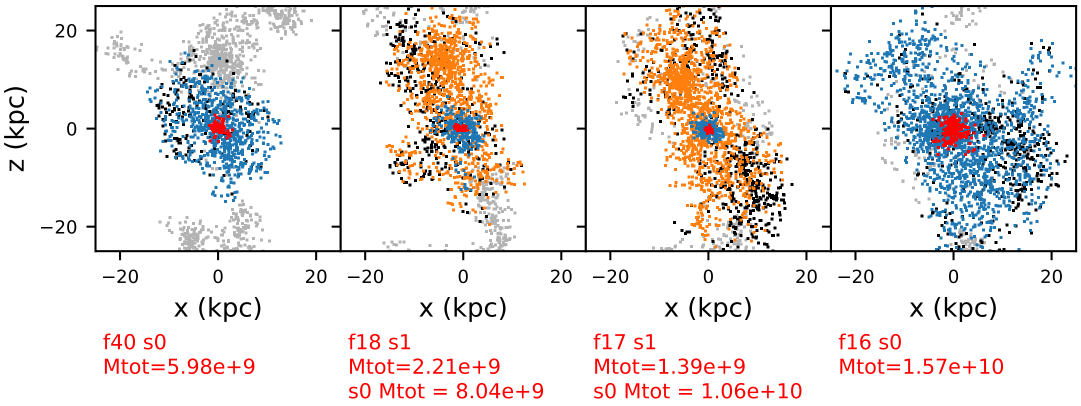

Figure 5.1: A characteristic example of the challenges we encountered when tracking galaxies back through time. Panels from left to right show the $x-z$ positions of dark matter particles near our subhalo of interest in snapshots 55, 58, 61, and 66, respectively. Colours indicate the subhalos to which particles belong. Blue points identify particles assigned to the halo/subhalo combination identified in the first stage of tracking (Section 5.1.1). Red points show the 10% most bound particles in that subhalo. Black indicate other subhalos in the same halo, and grey shows particles belonging to other halos. When the subhalo we are tracking is identified by subhalo number $s_i > 0$, the particles in subhalo $s_i = 0$ are coloured orange.
In snapshot 55 (leftmost panel), a clump can be seen approaching from the top of the image. In snapshots 58 and 61, Subfind identifies this clump and the majority of the original subhalo as one bound object with subhalo number $s_i = 0$, and the core dark matter particles are associated with a much smaller bound region, assigned $s_i = 1$. Finally, by snapshot 64 the errant clump has largely merged with the main structure, and our subhalo is once again $s_i = 0$.

We can catch the first case by applying a fix in cases where our subhalo is identified by $s_i > 0$. However, this is an imperfect solution, as there can be legitimate cases where a central is temporarily accreted by a larger object and then ejected again. In these cases, the subhalo *should* be assigned $s_i > 0$, and no anomalous properties would result.

The second case is much more challenging to identify, so some mass spikes will remain, whether we use Subfind's calculated galaxy properties or calculate them ourselves by summing particles within an aperture.

Method I: Modified Subfind Values

The fastest method for determining the evolution of galactic properties is simply to utilise the values calculated by Subfind. This does not require any calculation or particle indexing. To account for the issues discussed above, we do not trust Subfind's values at any snapshots where the subhalo number $s_i > 0$. Instead, at those snapshots, we calculate R_{200} and determine galaxy properties from the particles contained within it.

Method II: Calculated by Hand

The second method is to calculate galaxy properties by hand at every snapshot. For simplicity, in cases where $s_i = 0$, we use Subfind's value of R_{200}. Halo and gas masses are defined as the sum of masses within R_{200}, and stellar masses as the sum of stars within $R_{\mathrm{gal}} = 0.15 R_{200}$. When $s_i > 0$, we calculate R_{200} by hand.

In some cases, R_{200} cannot be robustly calculated. We thus apply a secondary constraint: if, when calculating R_{200}, it changes by more than 50% from the previous snapshot, we use the previous value instead of the calculated one.

The analysis presented in Section 5.2 uses data calculated by Method II. This has the advantange of being a more consistently defined value, in the sense that all properties are taken from within a spherical aperture scaled to the galaxy's size; it is also consistent with the definitions used in Chapter 4.

5.2 Investigating the Origins of SFH Mass-Dependence

5.2.1 Averaged Evolution by $z = 0$ Stellar Mass

An obvious first step in understanding the origins of present-day stellar mass is to compare the average evolution of several quantities of interest, for galaxies of different final masses.

We first plot the lifetime evolution of M_* and M_{200}, shown in Figure 5.2. Consistent with our previous findings, low-mass galaxies formed all of their stars early on, whereas more massive galaxies continue forming stars until significantly later (often right until $z = 0$). The growth of their host halos follows a similar, if less dramatic, trend.

We then compared the average behaviour of gas and baryonic mass components. The quantity that shows the most noteworthy variation with mass is the baryon

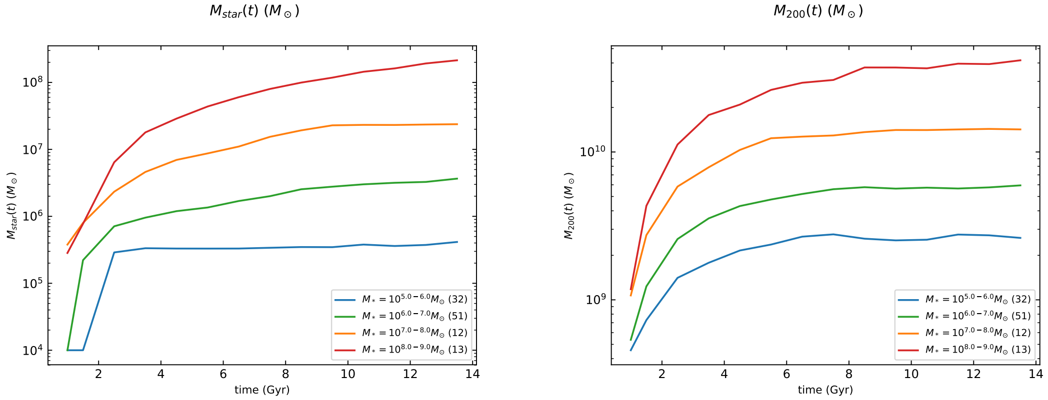

Figure 5.2: Average evolution of M_* (left) and M_{200} (right) for Ap-L2 field dwarfs, in bins of M_* $(z = 0)$. As seen in Chapter 4, low-mass stars form all of their stars early on, whereas more massive galaxies continue to grow until the present day. A similar, although less dramatic, trend is seen in the evolution of their halos.

fraction $M_{\rm bar} / M_{200}$: while galaxies with high $z = 0$ stellar masses maintain a near-constant baryon fraction throughout the entire simulation, low-mass galaxies experience significant baryon loss. This trend is shown in Figure 5.3.

Baryon loss from low-mass halos likely explains the differences in $z = 0$ stellar mass. But what causes some galaxies to lose more baryons than others? Two likely culprits are stellar feedback and the shallower potential wells of lower-mass galaxies. We attempt to disentangle these effects in the next section.

5.2.2 Isolating the Effects of Stellar Feedback

The majority of our dwarfs are found in low-mass halos, $M_{200} \sim 10^{9-9.5}\mathrm{M}_\odot$. At this mass, many halos are 'dark,' i.e., they do not contain any stars. Clearly, these halos cannot be subject to stellar feedback. We can thus attempt to determine the relative importance of stellar feedback on halo baryon fraction by comparing the evolution of luminous and dark halos of similar masses.

However, this picture is complicated by the fact that several processes can reduce baryon content in dark halos. Benítez-Llambay et al. (2017) introduced the useful categorization of dark subhalos as 'RELHICs' (REionization-Limited HI Clouds) or 'COSWEBs' (COSmic WEB stripped systems). Both categories of subhalo are dark due to the gas heating and subsequent baryon loss induced by cosmic reionization. Their differences arise from post-reionization evolution: COSWEBs are stripped by

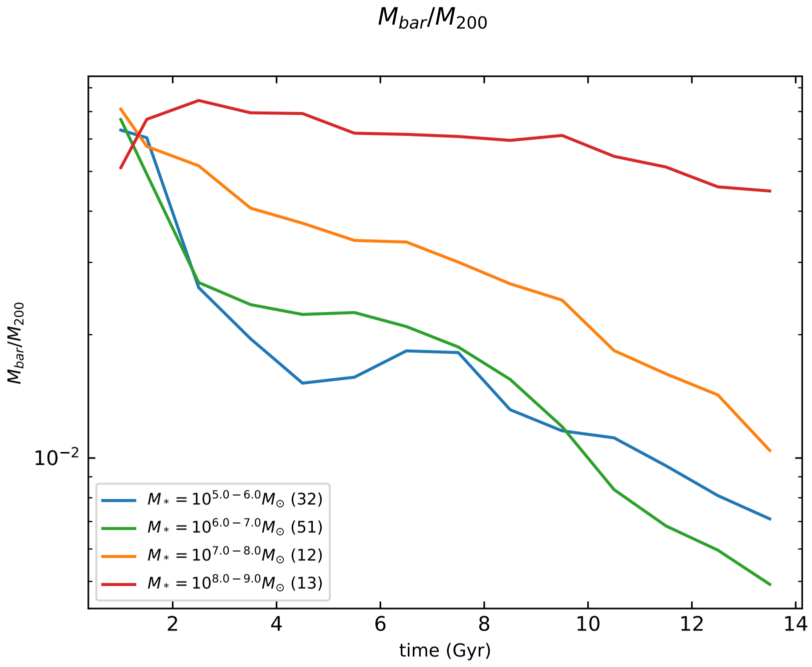

Figure 5.3: Average evolution of the fraction M_{bar}/M_{200} (baryon mass normalized by halo mass) for Ap-L2 field dwarfs. Lines correspond to M_* $(z = 0)$. The galaxies that have lower stellar masses at $z = 0$ are those which lose significant quantities of baryons; galaxies with high $z = 0$ stellar masses retain a roughly constant baryon fraction over time.

interaction with the cosmic web, leaving them nearly gasless, whereas RELHICs avoid these interactions and retain higher baryon fractions. As a result, baryon loss may be a result of halo mass (e.g. via heating from reionization, or due to a mass-dependent gas accretion rate), but it may also be due to environmental interactions.

In the following analysis, we attempt to distinguish RELHICs and COSWEBs based on surviving gas mass. It can be difficult to determine whether or not the gas in a subhalo's immediate vicinity is bound, so we do not impose a strict definition of COSWEBs as being completely gas-free. Instead, based on the distribution of the gas fraction $f_{gas} \equiv M_{\rm gas}/M_{200}$, we define COSWEBs as dark halos with $f_{gas} < 0.002$, and RELHICs as dark halos with $f_{gas} > 0.002$. We further restrict our analysis to those halos with M_{200} $(z = 0) > 10^9 {\rm M}_\odot$ to avoid 'backsplash' halos (those which have been accreted and then ejected by a primary), whose halo masses are frequently reduced by tidal stripping.

We next select a narrow range of initial halo masses, in order to compare the evolution of halos with similar initial properties. All but two of our halos containing luminous galaxies had masses in the range $10^{8.0} < M_{200}/{\rm M}_\odot < 10^{9.5}$ at $t = 1$ Gyr (the earliest time for which we have data). Of these halos, we select the mass range $10^{8.5} < M_{200}/{\rm M}_\odot < 10^{9.0}$ as it encompasses the greatest range of final stellar masses.

Figure 5.4 shows the evolution of M_{200}, M_*, and $M_{\rm bar}/M_{200}$ for halos with our selected narrow range of initial masses. These halos are divided into categories according to their final stellar mass and, for the dark halos, according to their final gas fraction.

The third panel of Figure 5.4 compares the evolution of $M_{\rm bar}/M_{200}$ in dark and luminous low-mass halos. As expected, COSWEBs lose a significant fraction of their baryons early on due to stripping by the cosmic web. RELHICs retain much higher gas fractions, with an average lifetime evolution of $M_{\rm bar}/M_{200}$ quite similar to that of the intermediate-mass luminous halos.

Relative to the RELHICs, low-mass luminous halos experience a period of rapid baryon loss in the first few Gyr. Given that dark halos do not experience similar baryon loss, it is likely a result of energetic feedback from the first generation of star formation. In addition, this phase of baryon loss is quite similar to that seen in the COSWEBs. It may be that, in some halos, gas heated by stellar feedback is then stripped by interactions with the cosmic web.

Medium-mass luminous halos lose a smaller fraction of their baryons; the increase in baryon retention may be due to their deeper potential wells and correspondingly

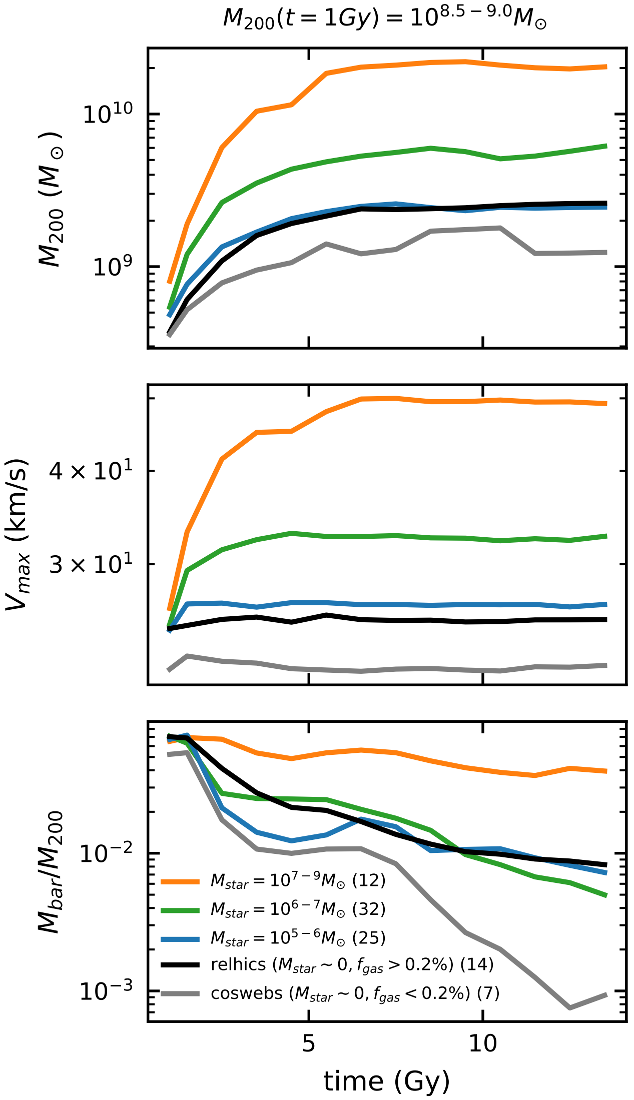

Figure 5.4: Comparing the evolution of dark and luminous halos. From top to bottom, the evolution of M_{200}, M_*, and $M_{\rm bar}/M_{200}$ for all halos in our sample with M_{200} ($t =$ 1Gyr) $= 10^{8.5-9.0}$M$_\odot$. Coloured lines indicate M_* ($z = 0$): grey and black indicate COSWEBs and RELHICs respectively; blue, green, and orange lines show luminous halos of increasing stellar mass. Although all 5 categories start with similar halo masses and baryon fractions, their evolution differs significantly. COSWEBs lose the majority of their baryons early on, through cosmic web stripping. Halos hosting low- and medium-mass galaxies also experience significant baryon loss, likely due to energetic feedback from the first generation of stars. The most massive galaxies, which form in the most massive halos, retain nearly all of their baryons.

stronger restoring forces, which prevents gas heated by feedback from escaping. This final point relies on the observation that, despite having similar masses at early times, the halo populations in Figure 5.4 rapidly diverge. Halos that end up more massive at $z = 0$ were more massive, and had higher values of $V_{\rm max}$, for the majority of their evolution. Is this simply an expression of the stellar mass - halo mass relation, or does a halo's size (as expressed by its mass or maximum circular velocity) at early times predict its final stellar mass more robustly than its size at $z = 0$ can alone?

5.2.3 Predictors of M_* $(z = 0)$

To first order, galactic evolution (including M_* $(z = 0)$) is a function of halo mass. However, there is a great deal of scatter in the SMHM relation, particularly at the low-mass end: halos of a given mass can contain galaxies that scatter over 1-2 dex in stellar mass, or may never have formed stars at all (see Figure 5.5). If we can identify a secondary parameter that drives the scatter in the SMHM relation, we can combine this parameter with halo mass to more tightly predict a galaxy's final stellar mass.

In Figure 5.4, although halos were selected to lie in a narrow range of masses at $t = 1$ Gyr, their sizes (as expressed by mass and $V_{\rm max}$) rapidly diverged. The result is a systematic trend between halo size at early times and stellar mass at $z = 0$. In the rest of this section, we investigate whether $V_{\rm max}(t = t_i)$ can be used to predict M_* $(z = 0)$. In particular, we measure $V_{\rm max}$ at $t_i = 3$ Gyr. 3 Gyr was selected as one of the earliest times at which $V_{\rm max}$ is clearly resolved by the simulations.

A qualitative look at the role of $V_{\rm max}(t = 3\,{\rm Gyr})$ is shown in Figure 5.6. This figure plots the evolution of M_{200} and M_* for individual halos occupying narrow ranges of M_{200} at $z = 0$. The evolutionary tracks are coloured by $V_{\rm max}(t = 3\,{\rm Gyr})$. Two features are of note. First, in such narrow M_{200} slices, there is not a strong correlation between $V_{\rm max}(t = 3\,{\rm Gyr})$ and M_{200} $(z = 0)$. This means that any trends between $V_{\rm max}(t = 3\,{\rm Gyr})$ and M_* $(z = 0)$ are not simply a reflection of the SMHM relation. Second, there *does* appear to be a correlation between $V_{\rm max}(t = 3\,{\rm Gyr})$ and M_* $(z = 0)$, at least for relatively high-mass halos.

Encouraged by Figures 5.4 and 5.6, we attempt to quantify the dependence of M_* $V_{\rm max}(t = 3\,{\rm Gyr})$ by comparing the relationships M_{200}-M_* and M_{200}-$V_{\rm max}(t = 3\,{\rm Gyr})$. Both relationships can be fit by a power law in the dwarf galaxy regime. If the residuals in these figures are correlated, this indicates that – at a fixed M_{200} – galaxies that collapsed earlier have higher stellar masses at $z = 0$. We should then be able to

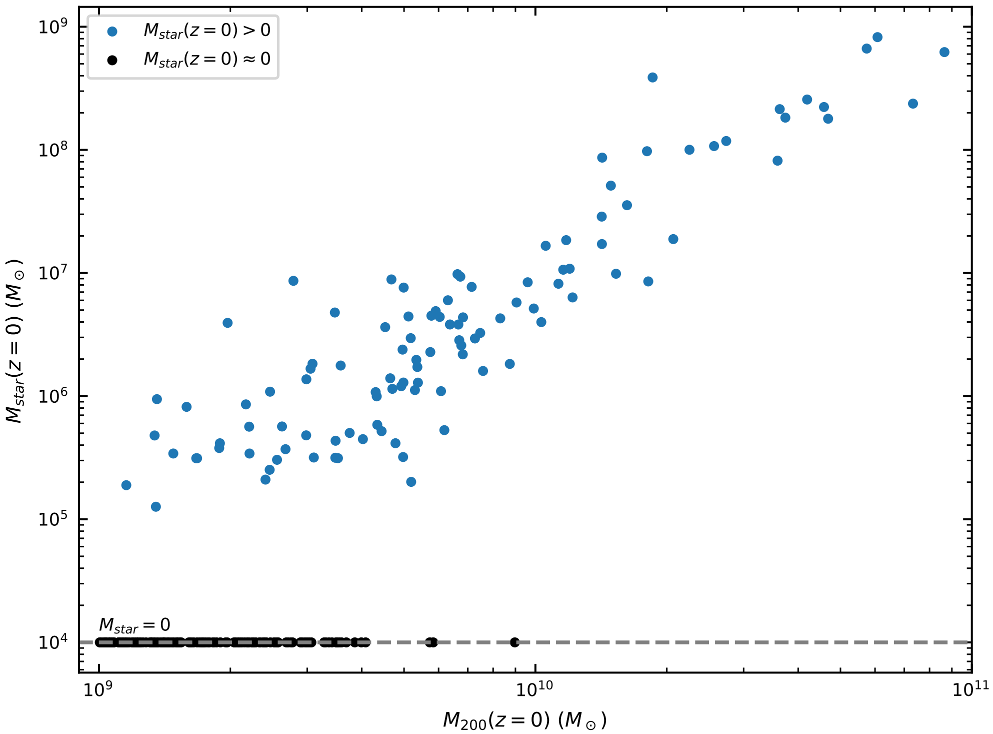

Figure 5.5: The SMHM relation for dwarf galaxies in Ap-L2. Luminous halos are shown in blue, and dark halos (those which have not formed any stars) are indicated in black, plotted at $M_* = 10^4 \mathrm{M}_\odot$ for the sake of illustration. The sample is restricted to halos with $M_{200} > 10^9 \mathrm{M}_\odot$. Because this figures contains only the dwarf galaxies ($M_* < 10^{11} \mathrm{M}_\odot$), the characteristic knee at higher masses is not visible.

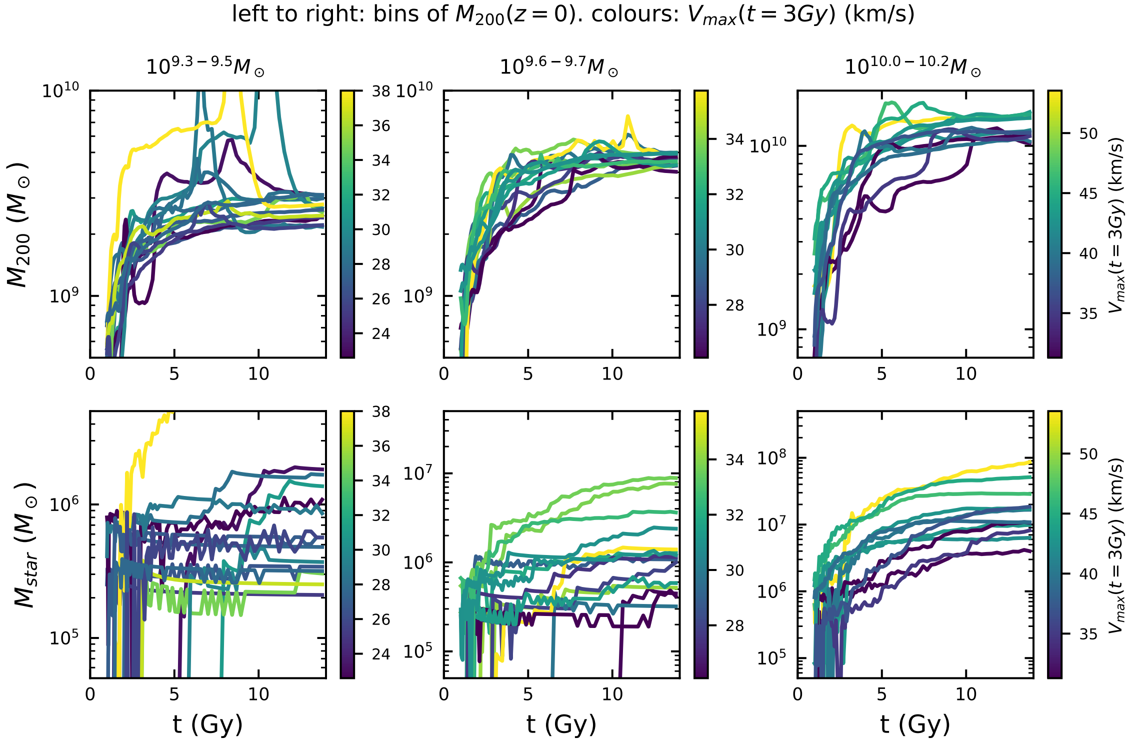

Figure 5.6: Evolution of individual galaxies in narrow bins of M_{200}. *Top:* M_{200} (t). *Bottom:* M_* (t). Lines are coloured by $V_{\rm max}(t = 3\,{\rm Gyr})$. Note in particular the correlation between $V_{\rm max}(t = 3\,{\rm Gyr})$ and M_* $(z = 0)$ in high-mass halos, where $V_{\rm max}$ was best resolved at early times.

find a combination of M_{200} and $V_{\rm max}(t = 3\,{\rm Gyr})$ that predicts M_* more tightly than M_{200} alone can. This relationship is equivalent to a rotation in three-dimensional M_{200}-$V_{\rm max}(t = 3\,{\rm Gyr})$-$M_*$ space.

Figure 5.7 shows our efforts to this end. The top panels show the M_{200} $(z = 0)$ – M_* $(z = 0)$ and M_{200} $(z = 0)$ – $V_{\rm max}(t = 3\,{\rm Gyr})$ relations, and the residuals of the two fits plotted against each other. A correlation can readily be seen: at a given halo mass, galaxies with higher stellar masses today tended to have higher values of $V_{\rm max}$ at $t = 3$ Gyr.

In the bottom panels of Figure 5.7, we plot the same data in a coordinate system which has been rotated $\sim 72\,{\rm deg}$ in the M_{200}-$V_{\rm max}(t = 3\,{\rm Gyr})$ plane to define $x' = 0.31\log M_{200} + 0.95\log V_{\rm max}(t = 3Gyr)$, $y' = -0.95\log M_{200} + 0.31\log V_{\rm max}(t = 3Gyr)$. The scatter in the x'-M_* relation is significantly reduced compared to that in the original M_{200} $(z = 0)$ - M_* $(z = 0)$ relation (from a standard deviation of 0.35 to 0.28) and the residuals between the two fits are de-correlated.

We include for this analysis only dwarfs with M_* $(z = 0) > 10^6{\rm M}_\odot$; at lower masses, the residuals did not correlate, and repeating this analysis with the full population of dwarfs did not obviously reduce the scatter in the transformed x'-M_* relation. This may be due to numerical effects, as such low-mass objects were resolved with very few particles at early times.

Finally, we consider the difference between luminous and dark halos. If cosmic reionization is expected to have evaporated the gas out of halos with $T_{vir} < 10^4 K$ at $z_{\rm reion}$, it seems plausible that halo properties at some later time would also correlate with star formation or the lack thereof. Indeed, in Figure 5.4, dark halos had consistently lower average values of $V_{\rm max}$ than luminous halos did.

We plot the distribution of $V_{\rm max}(t = 3\,{\rm Gyr})$ for dark and luminous halos with $10^{9.0} < M_{200}/{\rm M}_\odot < 10^{9.5}$ in Figure 5.8. The distributions are clearly offset, with a median $V_{\rm max}(t = 3\,{\rm Gyr})$ of 19.2 km/s and 27.4 km/s in dark and luminous halos, respectively. However, there is overlap between the two populations. Halo $V_{\rm max}$ at early times is indicative, but not conclusive, in predicting whether halos will have formed any stars.

5.3 Summary: The Origins of SFH Trends in Simulated Field Dwarfs

We conclude this chapter by referring once again to Figure 5.4, which succinctly expresses our main results.

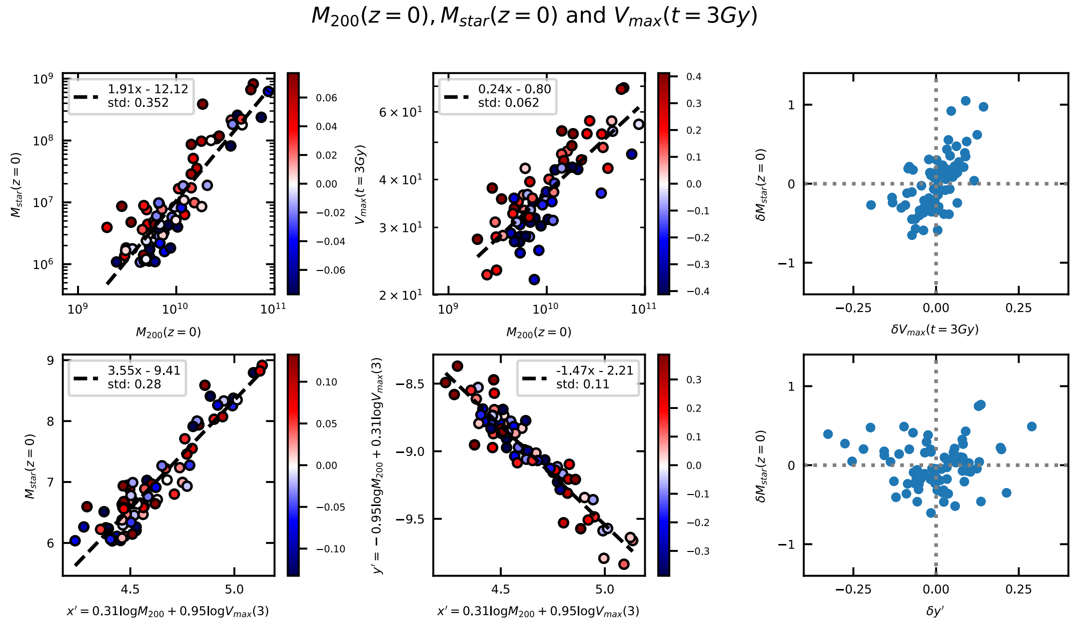

Figure 5.7: *Top row*: M_{200} $(z = 0)$ vs M_* $(z = 0)$ (left) and $V_{\rm max}(t = 3\,{\rm Gyr})$ (centre), each plot coloured by the residuals in the other; and those residuals plotted against each other (right). *Bottom row:* the same but for a rotated coordinate frame, with $x' = 0.31\,\log M_{200}\ +0.95\,\log V_{\rm max}(t = 3Gyr)$. Note that this rotated coordinate frame significantly reduces the correlation between the residuals of the two plots, and that the scatter in x'-M_* is reduced from that in M_{200}-M_*. These panels only include dwarfs with M_* $(z = 0) > 10^6{\rm M}_\odot$.

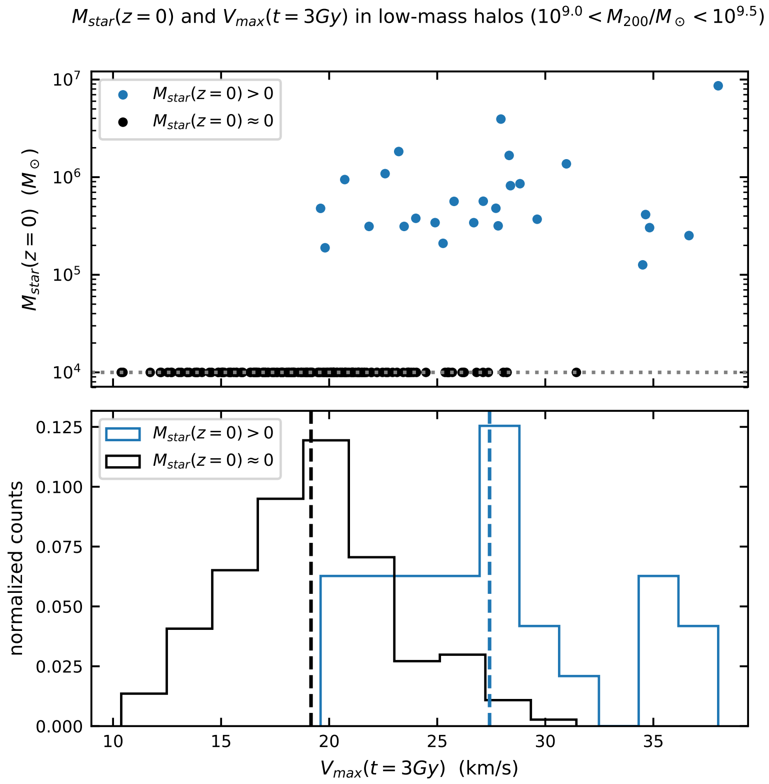

Figure 5.8: In low-mass halos ($10^{9.0} < M_{200}/\mathrm{M}_\odot < 10^{9.5}$), the absence or presence of star formation seems to be set by halo size at early times. The median $V_{\max}(t = 3\,\mathrm{Gyr})$ in dark and luminous halos was 19.2 km/s and 27.4 km/s, respectively.

In an effort to understand the origins of the trends in SFH with stellar mass presented in Chapter 4, we have analyzed the lifetime evolution of Ap-L2 field dwarfs. The final panel of Figure 5.4 shows that the galaxies with low present-day stellar masses are those which lose significant baryons in the first few Gyrs of their evolution. Deprived of fuel for star formation, these galaxies cannot continue to form stars. More massive galaxies, which tend to inhabit more massive halos, retain their baryons more effectively and can continue star formation until the present day.

Comparing the evolution of dark and luminous halos in Figure 5.4, it seems likely that the baryon loss in low-mass galaxies is a result of stellar feedback from the first generation of stars, possibly in combination with stripping induced by interactions with the cosmic web. Dark halos which are not stripped by interactions with the cosmic web do not experience a similar baryon loss at early times.

Finally, the properties of halos at early times appear to predict their present-day stellar content. On average, halos that do not contain any stars had lower values of V_{max} at $t = 3$ Gyr that those that contain galaxies. Further, at fixed halo mass, galaxies with higher values of V_{max} at $t = 3$ Gyr tend to have higher stellar masses by $z = 0$.

Chapter 6

Parting Thoughts

6.1 Thesis Summary

This thesis has detailed my research on the star formation histories (SFHs) of dwarf galaxies in Local Group-like environments. I used the APOSTLE and Auriga simulations, in conjunction with published observations of the Local Group, to characterize the impact of stellar mass and environment on dwarf SFHs. I then analyzed the lifetime evolution of simulated APOSTLE field dwarfs to understand the origins of the mass dependence of these SFHs.

My main results can be summarized as follows:

- The SFHs of APOSTLE and Auriga dwarfs are in remarkable agreement, despite these simulations using markedly different computational techniques.
- These SFHs are characterized by remarkable diversity, even amongst dwarfs of similar mass and environment.
- On average, the SFHs of isolated field dwarfs exhibit clear trends with stellar mass. Low-mass galaxies form all of their stars in the first few Gyr, then stop; increasing $z = 0$ stellar mass corresponds to increasingly extended SFHs, with the most massive dwarfs still forming stars at the present day.
- Satellite dwarfs exhibit similar average trends with stellar mass, except for a substantial suppression in late-time star formation.
- Observational SFHs derived from colour-magnitude diagrams (CMDs) are consistent with those found in simulations, when the observations reach sufficient photometric depth to resolve the oldest main-sequence turnoff (oMSTO).

- Observational SFHs derived from shallow data that does not resolve the oMSTO is substantially more prone to systematics, and tends to under-emphasize the importance of star formation at intermediate epochs. Caution is advised when interpreting the relative distribution of early and intermediate star formation in these shallow observations.

- Baryon loss from low-mass halos appears to explain the early cessation of star formation in low-mass field dwarfs. Comparison with dark (starless) halos suggests that this baryon loss is likely due to energetic feedback from the first generations of stars, possibly in combination with stripping induced by interaction with the cosmic web.

6.2 Future Prospects

Having established the *average* dependence of dwarf galaxy evolution on stellar mass and environment, the next question is whether we can explain the *diversity* of dwarf SFHs. Is each galaxy's SFH the product of its individual history, driven by chance encounters with other galaxies and the cosmic web? Or, given a galaxy's initial properties and environment, can we make predictions about its $z = 0$ characteristics relative to a 'typical' dwarf of its mass?

Addressing these questions will entail a more detailed analysis of the lifetime evolution of dwarf galaxies in cosmological simulations, studied both individually and as ensembles. Fortunately, there are a wealth of such simulations, with numerical methods under constant development. Comparing the evolution of dwarfs across simulations will be an important part of this process, as numerical effects and differences in the implementation of subgrid physics can have influence significantly the evolution of such small objects. For example, our results suggest that energetic feedback from the early generations of star formation is responsible for suppressing star formation in low-mass dwarfs; it is therefore vital that we understand whether this result changes with different subgrid recipes for feedback.

Additional insight will come with the next generations of dwarf observations. Deeper photometry, capable of resolving the oldest main sequence turnoff, is required to constrain the early epochs of star formation. Broader photometry, covering greater fractions of dwarfs' spatial extent, is also vital to capture radial gradients in age and star formation. It is of course infeasible to attempt both of these extensions to our current data simultaneously, but studies on the typical impact of increasing depth or extent (such as those comparisons already published in Weisz et al. (2011)) will be extremely informative.

Appendix A

Supplementary Material

A.1 Observational Data Tables

Tables A.1 and A.2 list the properties of observed field dwarfs and satellites, respectively, used in our analysis. Galaxies are listed alphabetically by name. Values of $f_{1\mathrm{Gy}}$ and τ_{90} are only computed for galaxies that resolve the oMSTO.

Table A.1: Data values for the observed *field* galaxies.

Gal. Name	BMag (mag)	Mstar ($M_\odot$)	$f_{1\rm Gy}$	$f_{4\rm Gy}$	$f_{8\rm Gy}$	τ_{90} (Gy)	oMSTO	Ref.
A0952+69	-11.5	5.97e+06	-	$0.4^{+-0.29}_{-0.0}$	$0.43^{+-0.06}_{-0.0}$	-	n	W11
AndXXVIII	-7.7	1.80e+05	$0.54^{+0.11}_{-0.09}$	$0.73^{+-0.62}_{-0.6}$	$0.96^{+-0.95}_{-0.96}$	$6.13^{+0.28}_{-1.75}$	y	S17
Antlia	-9.8	1.25e+06	-	$0.18^{+0.06}_{-0.05}$	$0.45^{+-0.11}_{-0.27}$	-	n	W11
Aquarius	-11.1	4.13e+06	$0.05^{+0.01}_{-0.02}$	$0.14^{+-0.08}_{-0.1}$	$0.67^{+-0.63}_{-0.59}$	$11.1^{+0.02}_{-0.04}$	y	C14
BK3N	-9.6	1.04e+06	-	$0.41^{+-0.35}_{-0.32}$	$0.46^{+-0.05}_{-0.25}$	-	n	W11
BK5N	-10.6	2.61e+06	-	$0.93^{+-0.88}_{-0.0}$	$0.93^{+-0.87}_{-0.76}$	-	n	W11
Cetus	-10.2	1.80e+06	$0.12^{+0.11}_{-0.16}$	$0.86^{+-0.75}_{-0.75}$	$0.96^{+-0.94}_{-0.91}$	$4.38^{+0.63}_{-1.03}$	y	G15
DDO113	-11.5	5.97e+06	-	$0.58^{+-0.35}_{-0.02}$	$0.59^{+-0.33}_{-0.36}$	-	n	W11
DDO125	-14.3	7.87e+07	-	$0.46^{+-0.02}_{-0.0}$	$0.97^{+-0.94}_{-0.82}$	-	n	W11
DDO155	-12.0	9.46e+06	-	$0.6^{+-0.36}_{-0.36}$	$0.71^{+-0.54}_{-0.58}$	-	n	W11
DDO165	-15.1	1.64e+08	-	$0.54^{+-0.23}_{-0.0}$	$0.57^{+-0.28}_{-0.0}$	-	n	W11
DDO181	-13.2	2.86e+07	-	$0.72^{+-0.52}_{-0.0}$	$0.72^{+-0.57}_{-0.53}$	-	n	W11
DDO183	-13.2	2.86e+07	-	$0.66^{+-0.48}_{-0.22}$	$0.68^{+-0.51}_{-0.58}$	-	n	W11
DDO187	-12.4	1.37e+07	-	$0.45^{+-0.27}_{-0.07}$	$0.48^{+-0.24}_{-0.27}$	-	n	W11
DDO190	-14.1	6.55e+07	-	$0.33^{+0.14}_{-0.17}$	$0.43^{+-0.08}_{-0.25}$	-	n	W11
DDO44	-12.1	1.04e+07	-	$0.34^{+0.16}_{-0.03}$	$0.39^{+0.13}_{-0.16}$	-	n	W11
DDO53	-13.4	3.44e+07	-	$0.42^{+-0.09}_{-0.0}$	$0.58^{+-0.29}_{-0.01}$	-	n	W11
DDO6	-12.4	1.37e+07	-	$0.55^{+-0.26}_{-0.01}$	$0.58^{+-0.29}_{-0.21}$	-	n	W11
DDO71	-12.1	1.04e+07	-	$0.45^{+-0.06}_{-0.0}$	$0.66^{+-0.36}_{-0.43}$	-	n	W11
DDO78	-11.5	5.97e+06	-	$0.56^{+-0.34}_{-0.26}$	$0.58^{+-0.37}_{-0.34}$	-	n	W11

Table A.1 – (continued)

Gal. Name	BMag	$(\mathrm{M}_\odot)$				(Gy)		
DDO82	-14.7	1.14e+08	-	$0.47^{+-0.33}_{-0.31}$	$0.52^{+-0.23}_{-0.34}$	-	n	W11
DDO99	-13.5	3.77e+07	-	$0.76^{+-0.64}_{-0.44}$	$0.93^{+-0.9}_{-0.88}$	-	n	W11
ESO269-037	-12.0	9.46e+06	-	$0.94^{+-0.89}_{-0.31}$	$0.94^{+-0.91}_{-0.84}$	-	n	W11
ESO294-010	-10.9	3.44e+06	-	$0.8^{+-0.71}_{-0.56}$	$0.87^{+-0.79}_{-0.61}$	-	n	W11
ESO321-014	-12.7	1.80e+07	-	$0.77^{+-0.61}_{-0.11}$	$0.83^{+-0.7}_{-0.41}$	-	n	W11
ESO325-011	-14.0	5.97e+07	-	$0.59^{+-0.25}_{-0.26}$	$0.69^{+-0.46}_{-0.48}$	-	n	W11
ESO383-087	-17.0	9.46e+08	-	$0.71^{+-0.56}_{-0.15}$	$0.91^{+-0.87}_{-0.72}$	-	n	W11
ESO410-005	-11.6	6.55e+06	-	$0.63^{+-0.46}_{-0.47}$	$0.8^{+-0.7}_{-0.69}$	-	n	W11
ESO540-030	-11.4	5.45e+06	-	$0.02^{+0.6}_{-0.02}$	$0.08^{+0.36}_{-0.02}$	-	n	W11
ESO540-032	-11.3	4.97e+06	-	$0.86^{+-0.75}_{-0.01}$	$0.86^{+-0.76}_{-0.7}$	-	n	W11
F8D1	-12.6	1.64e+07	-	$0.65^{+-0.31}_{-0.47}$	$0.66^{+-0.33}_{-0.55}$	-	n	W11
FM1	-10.5	2.38e+06	-	$0.89^{+-0.81}_{-0.66}$	$0.9^{+-0.83}_{-0.74}$	-	n	W11
HS117	-11.2	4.53e+06	-	$0.83^{+-0.74}_{-0.48}$	$0.83^{+-0.76}_{-0.74}$	-	n	W11
HoI	-14.5	9.46e+07	-	$0.0^{+0.59}_{-0.0}$	$0.06^{+0.66}_{-0.0}$	-	n	W11
HoII	-16.7	7.18e+08	-	$0.81^{+-0.7}_{-0.22}$	$0.81^{+-0.75}_{-0.69}$	-	n	W11
HoIX	-13.6	4.13e+07	-	$0.27^{+0.27}_{-0.07}$	$0.73^{+-0.53}_{-0.44}$	-	n	W11
IC1613	-14.5	9.46e+07	$0.05^{+0.11}_{-0.16}$	$0.39^{+-0.28}_{-0.29}$	$0.7^{+-0.68}_{-0.65}$	$11.46^{+0.63}_{-1.03}$	y	G15
IC2574	-17.5	1.50e+09	-	$0.86^{+-0.76}_{-0.47}$	$0.86^{+-0.81}_{-0.75}$	-	n	W11
IC5152	-15.6	2.61e+08	-	$0.35^{+-0.12}_{-0.11}$	$0.82^{+-0.69}_{-0.8}$	-	n	W11
IKN	-11.6	6.55e+06	-	$0.92^{+-0.84}_{-0.23}$	$0.95^{+-0.92}_{-0.82}$	-	n	W11
KDG52	-11.5	5.97e+06	-	$0.93^{+-0.87}_{-0.19}$	$0.93^{+-0.87}_{-0.67}$	-	n	W11
KDG61	-12.9	2.17e+07	-	$0.63^{+-0.36}_{-0.0}$	$0.64^{+-0.4}_{-0.21}$	-	n	W11

Table A.1 – (continued)

Gal. Name	BMag	(M$_\odot$)				(Gy)		
KDG64	-12.6	1.64e+07	-	$0.48^{+-0.07}_{-0.14}$	$0.59^{+-0.27}_{-0.38}$	-	n	W11
KDG73	-10.8	3.13e+06	-	$0.3^{+0.05}_{-0.01}$	$0.36^{+0.2}_{-0.0}$	-	n	W11
KK077	-12.0	9.46e+06	-	$0.49^{+-0.21}_{-0.28}$	$0.76^{+-0.55}_{-0.56}$	-	n	W11
KKH37	-11.6	6.55e+06	-	$0.45^{+-0.11}_{-0.01}$	$0.52^{+-0.25}_{-0.25}$	-	n	W11
KKH86	-10.3	1.98e+06	-	$0.71^{+-0.52}_{-0.09}$	$0.82^{+-0.7}_{-0.24}$	-	n	W11
KKH98	-10.8	3.13e+06	-	$0.22^{+0.12}_{-0.02}$	$0.64^{+-0.35}_{-0.19}$	-	n	W11
KKR25	-9.4	8.63e+05	-	$0.58^{+-0.26}_{-0.0}$	$0.62^{+-0.35}_{-0.18}$	-	n	W11
KKR3	-9.2	7.18e+05	-	$0.76^{+-0.64}_{-0.37}$	$0.77^{+-0.65}_{-0.6}$	-	n	W11
LeoA	-11.7	7.18e+06	$0.0^{+0.11}_{-0.16}$	$0.05^{+0.06}_{--0.05}$	$0.37^{+-0.35}_{-0.32}$	$12.55^{+0.63}_{-1.03}$	y	G15
LeoT	-6.7	7.18e+04	$0.41^{+0.12}_{-0.21}$	$0.41^{+-0.27}_{-0.33}$	$0.72^{+-0.67}_{-0.62}$	$12.12^{+0.12}_{-0.06}$	y	W14
NGC2366	-16.1	4.13e+08	-	$0.67^{+-0.48}_{-0.0}$	$0.68^{+-0.53}_{-0.5}$	-	n	W11
NGC3109	-15.7	2.86e+08	-	$0.79^{+-0.67}_{-0.0}$	$0.79^{+-0.69}_{-0.62}$	-	n	W11
NGC3741	-13.1	2.61e+07	-	$0.68^{+-0.48}_{-0.3}$	$0.7^{+-0.53}_{-0.46}$	-	n	W11
NGC4163	-13.8	4.97e+07	-	$0.48^{+-0.33}_{-0.19}$	$0.92^{+-0.86}_{-0.65}$	-	n	W11
NGC4228	-17.2	1.14e+09	-	$0.73^{+-0.52}_{-0.0}$	$0.95^{+-0.92}_{-0.82}$	-	n	W11
NGC55	-18.4	3.44e+09	-	$0.63^{+-0.47}_{-0.38}$	$0.69^{+-0.52}_{-0.54}$	-	n	W11
NGC6822	-15.2	1.80e+08	-	$0.23^{+-0.12}_{-0.14}$	$0.36^{+0.05}_{-0.28}$	-	n	W14
PegasusdIrr	-11.5	5.97e+06	-	$0.54^{+-0.29}_{-0.13}$	$0.54^{+-0.24}_{-0.15}$	-	n	W14
Phoenix	-9.6	1.04e+06	$0.1^{+0.11}_{-0.16}$	$0.54^{+-0.43}_{-0.44}$	$0.82^{+-0.8}_{-0.77}$	$10.56^{+0.63}_{-1.03}$	y	G15
SagDIG	-11.5	5.97e+06	-	$0.38^{+-0.0}_{-0.0}$	$0.56^{+-0.25}_{-0.16}$	-	n	W14
Sc22	-10.5	2.38e+06	-	$0.72^{+-0.53}_{-0.01}$	$0.75^{+-0.56}_{-0.0}$	-	n	W11
SexA	-13.9	5.45e+07	-	$0.61^{+-0.44}_{-0.52}$	$0.71^{+-0.63}_{-0.64}$	-	n	W14

Table A.1 – (continued)

Gal. Name	BMag	($M_\odot$)				(Gy)		
SexB	-14.0	5.97e+07	-	$0.69^{+-0.48}_{-0.36}$	$0.83^{+-0.76}_{-0.73}$	-	n	W14
Tuc	-9.2	7.18e+05	$0.21^{+0.11}_{-0.16}$	$0.89^{+-0.78}_{-0.79}$	$0.95^{+-0.93}_{-0.9}$	$4.11^{+0.63}_{-1.03}$	y	G15
UA292	-11.8	7.87e+06	-	$0.45^{+-0.04}_{-0.0}$	$0.48^{+-0.11}_{-0.01}$	-	n	W11
UA438	-12.9	2.17e+07	-	$0.65^{+-0.43}_{-0.0}$	$0.93^{+-0.85}_{-0.8}$	-	n	W11
UGC4483	-12.7	1.80e+07	-	$0.07^{+0.51}_{-0.0}$	$0.91^{+-0.85}_{-0.86}$	-	n	W11
UGC8508	-13.1	2.61e+07	-	$0.58^{+-0.36}_{-0.01}$	$0.59^{+-0.34}_{-0.46}$	-	n	W11
UGC8833	-12.2	1.14e+07	-	$0.71^{+-0.55}_{-0.0}$	$0.73^{+-0.59}_{-0.6}$	-	n	W11
WLM	-14.1	6.55e+07	-	$0.34^{+-0.27}_{-0.24}$	$0.39^{+-0.3}_{-0.31}$	-	n	W14

References: Stellar masses are derived from B-magnitudes taken from Karachentsev et al. (2013), assuming a mass-to-light ratio of 1. We take star formation histories from the following references: W11: Weisz et al. (2011), W14: Weisz et al. (2014), C14: Cole et al. (2014), G15: Gallart et al. (2015), and S17: Skillman et al. (2017). Errors indicate the 16th and 84th percentile bounds on the combined random and systematic errors. SFHs published in Gallart et al. (2015) only quote random errors, whereas the others publish both random and systematic uncertainties; to be consistent in our analysis, we assign galaxies from Gallart et al. (2015) the median error range of the other oMSTO galaxies. These errors are $f_{1\mathrm{Gy}} = X^{+0.11}_{-0.16}$; τ_{90} /Gy = $\mathrm{Y}^{+0.63}_{-1.03}$.

Table A.2: Data values for the observed *satellite* galaxies.

Gal. Name	BMag (mag)	Mstar ($M_\odot$)	f_{1Gy}	f_{4Gy}	f_{8Gy}	τ_{90} (Gy)	oMSTO	Ref.
AndI	-10.7	2.86e+06	$0.55^{+0.04}_{-0.2}$	$0.61^{+-0.5}_{-0.44}$	$0.97^{+-0.96}_{-0.96}$	$6.29^{+0.67}_{-0.84}$	y	S17
AndII	-9.2	7.18e+05	$0.48^{+0.02}_{-0.15}$	$0.55^{+-0.45}_{-0.47}$	$0.93^{+-0.89}_{-0.9}$	$7.39^{+0.6}_{-0.51}$	y	S17
AndIII	-9.3	7.87e+05	$0.4^{+0.18}_{-0.15}$	$0.71^{+-0.45}_{-0.61}$	$0.96^{+-0.95}_{-0.96}$	$4.93^{+0.67}_{-1.47}$	y	S17
AndV	-9.2	7.18e+05	-	$0.72^{+-0.47}_{-0.43}$	$0.93^{+-0.91}_{-0.85}$	-	n	W14
AndVI	-10.7	2.86e+06	-	$0.55^{+-0.2}_{-0.46}$	$0.83^{+-0.77}_{-0.75}$	-	n	W14
AndVII	-11.7	7.18e+06	-	$0.98^{+-0.96}_{-0.92}$	$0.98^{+-0.96}_{-0.96}$	-	n	W14
AndXI	-6.2	4.53e+04	-	$0.78^{+-0.61}_{-0.52}$	$0.87^{+-0.79}_{-0.86}$	-	n	W14
AndXII	-6.4	5.44e+04	-	$0.4^{+-0.07}_{-0.21}$	$0.87^{+-0.76}_{-0.57}$	-	n	W14
AndXIII	-6.8	7.87e+04	-	$0.9^{+-0.86}_{-0.55}$	$0.9^{+-0.83}_{-0.81}$	-	n	W14
AndXV	-8.7	4.53e+05	$0.59^{+0.34}_{-0.17}$	$0.89^{+-0.82}_{-0.79}$	$0.94^{+-0.93}_{-0.94}$	$4.24^{+0.87}_{-3.13}$	y	S17
AndXVI	-8.2	2.86e+05	$0.48^{+0.06}_{-0.17}$	$0.5^{+-0.43}_{-0.39}$	$0.92^{+-0.9}_{-0.86}$	$7.88^{+0.56}_{-0.49}$	y	S17
CanVenI	-7.9	2.17e+05	$0.58^{+0.13}_{-0.11}$	$0.63^{+-0.4}_{-0.52}$	$0.99^{+-0.98}_{-0.94}$	$5.38^{+2.01}_{-1.13}$	y	W14
CanVenII	-4.1	6.55e+03	$0.24^{+0.16}_{-0.24}$	$0.73^{+-0.61}_{-0.42}$	$0.99^{+-0.99}_{-0.85}$	$5.42^{+3.59}_{-1.15}$	y	W14
Car	-9.0	5.97e+05	$0.26^{+0.06}_{-0.26}$	$0.46^{+-0.44}_{-0.21}$	$0.46^{+-0.29}_{-0.46}$	$11.46^{+0.07}_{-1.49}$	y	W14
Draco	-8.7	4.53e+05	$0.3^{+0.4}_{-0.2}$	$0.95^{+-0.92}_{-0.66}$	$0.97^{+-0.96}_{-0.95}$	$3.55^{+2.5}_{-1.52}$	y	W14
For	-11.5	5.97e+06	$0.18^{+0.13}_{-0.1}$	$0.29^{+-0.17}_{-0.2}$	$0.62^{+-0.55}_{-0.57}$	$11.46^{+0.2}_{-0.27}$	y	W14
Her	-6.1	4.13e+04	$0.91^{+0.08}_{-0.47}$	$0.91^{+-0.83}_{-0.71}$	$0.91^{+-0.82}_{-0.82}$	$1.11^{+9.77}_{-0.0}$	y	W14
IC10	-16.0	3.77e+08	-	$0.32^{+-0.17}_{-0.21}$	$0.32^{+-0.1}_{-0.2}$	-	n	W14
LGS3	-9.3	7.87e+05	$0.08^{+0.11}_{-0.16}$	$0.79^{+-0.68}_{-0.69}$	$0.9^{+-0.88}_{-0.85}$	$7.82^{+0.63}_{-1.03}$	y	G15
LeoI	-11.0	3.77e+06	$0.19^{+0.05}_{-0.19}$	$0.19^{+-0.09}_{-0.13}$	$0.48^{+-0.43}_{-0.41}$	$12.02^{+0.06}_{-0.2}$	y	W14

Table A.2 – (continued)

Gal. Name	BMag (mag)	Mstar ($M_\odot$)	f_{1Gy}	f_{4Gy}	f_{8Gy}	τ_{90} (Gy)	oMSTO	Ref.
LeoII	-9.1	6.55e+05	$0.13^{+0.07}_{-0.11}$	$0.33^{+-0.22}_{-0.24}$	$0.97^{+-0.96}_{-0.92}$	$7.29^{+0.6}_{-0.75}$	y	W14
LeoIV	-4.2	7.18e+03	$0.42^{+0.44}_{-0.25}$	$0.91^{+-0.83}_{-0.37}$	$0.91^{+-0.83}_{-0.76}$	$2.45^{+9.36}_{-0.92}$	y	W14
M32	-14.8	1.25e+08	-	$0.61^{+-0.49}_{-0.57}$	$0.77^{+-0.69}_{-0.64}$	-	n	W14
NGC147	-14.8	1.25e+08	-	$0.4^{+-0.08}_{-0.24}$	$0.75^{+-0.52}_{-0.56}$	-	n	W14
NGC185	-14.7	1.14e+08	-	$0.41^{+-0.05}_{-0.32}$	$0.82^{+-0.66}_{-0.74}$	-	n	W14
NGC205	-16.1	4.13e+08	-	$0.36^{+-0.03}_{-0.33}$	$0.83^{+-0.74}_{-0.72}$	-	n	W14
SagdSph	-12.7	1.80e+07	$0.14^{+0.0}_{-0.14}$	$0.14^{+0.05}_{-0.04}$	$0.48^{+-0.19}_{-0.35}$	$10.3^{+0.33}_{-1.82}$	y	W14
Sculptor	-9.8	1.25e+06	$0.2^{+0.6}_{-0.06}$	$0.96^{+-0.93}_{-0.79}$	$0.98^{+-0.96}_{-0.96}$	$3.09^{+3.53}_{-1.29}$	y	W14
UMi	-7.1	1.04e+05	$0.26^{+0.46}_{-0.03}$	$0.61^{+-0.27}_{-0.53}$	$0.97^{+-0.95}_{-0.91}$	$4.63^{+3.27}_{-1.6}$	y	W14

References: Stellar masses are derived from B-magnitudes taken from Karachentsev et al. (2013), assuming a mass-to-light ratio of 1. We take star formation histories from the following references: W11: Weisz et al. (2011), W14: Weisz et al. (2014), G15: Gallart et al. (2015), and S17: Skillman et al. (2017). Errors indicate the 16th and 84th percentile bounds on the combined random and systematic errors.

A.2 Detailed Auriga Results

Figures 4.3-4.6 in the main text compare observations with simulation data from Ap-L1. We include here the same figures, but with data from the Auriga simulation Au-L3. The trends in Au-L3 reproduce well those seen in Ap-L1, and are also seen in the lower-resolution Au-L4.

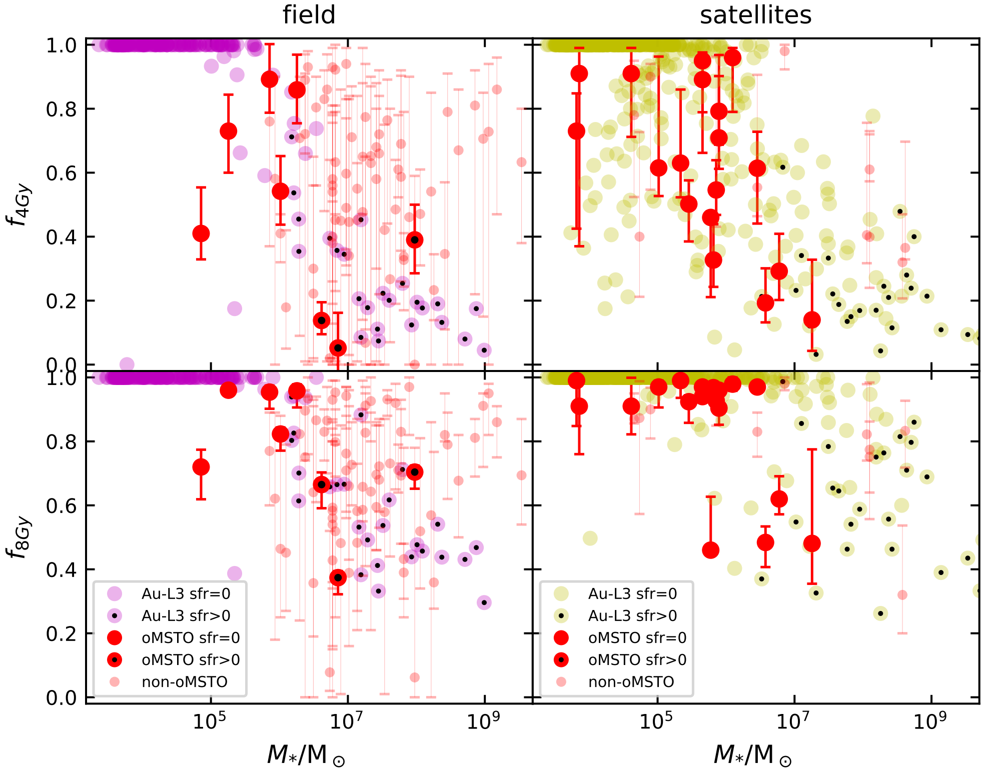

Figure A.1: As Fig. 4.3, but with Au-L3 data: The cumulative fraction of stars formed in the first 4 ($f_{\rm 4Gy}$) and 8 ($f_{\rm 8Gy}$) Gyr of cosmic evolution, as a function of stellar mass. Auriga galaxies are shown in magenta (field dwarfs) and yellow (satellites); observed galaxies are in red. Error bars in the latter indicate the 16th and 84th percentile bounds on the combined statistical and systematic uncertainties, as given in the literature (see Tables A.1 and A.2). Filled red circles highlight observed galaxies where the photometry reaches the oldest main sequence turnoff.

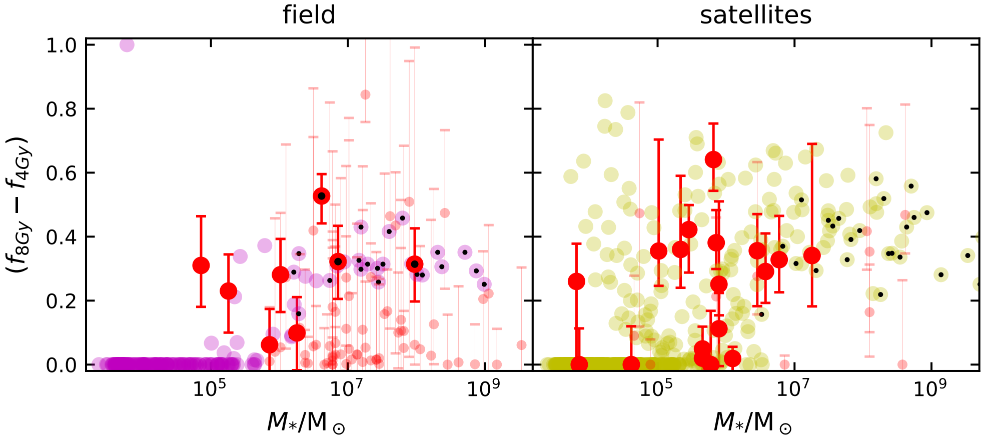

Figure A.2: As Fig. A.1, but for the difference between the fraction of stars formed by the first 4 and 8 Gyrs of cosmic evolution.

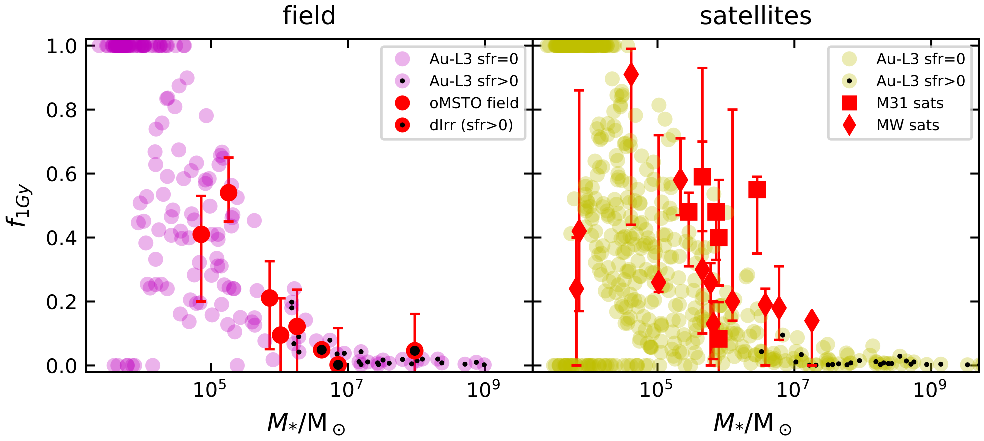

Figure A.3: As Fig 4.5, but with Au-L3 data: The fraction of stars formed in the first ~ 1 Gy of cosmic evolution, as a function of stellar mass. Error bars indicate the 16th and 84th percentile bounds on the combined statistical and systematic uncertainties, as published in the literature. Symbols differentiate observed field dwarfs (circles) from satellites of M31 (squares) and of the Milky Way (diamonds). Black dots indicate the observed dIrrs Aquarius, IC1613, and LeoA, which are still forming stars at the present day. Au-L3 field results are a closer match to the observations than the Apostle galaxies shown in Fig 4.5; Ap-L1 results were dominated by $f_{1\mathrm{Gy}} \sim 0$ at low masses, likely due to the choice of reionization redshift. Like Apostle, Au-L3 satellites show a slight but systematic shift toward lower values of $f_{1\mathrm{Gy}}$ or M_*. Possible reasons for this include the effects of tidal stripping, or, more likely, inaccuracies related to numerical limitations. Note that galaxies with $M_* < 10^5 \mathrm{M}_\odot$ are resolved with ~ 15 particles or fewer, and are included only for illustration.

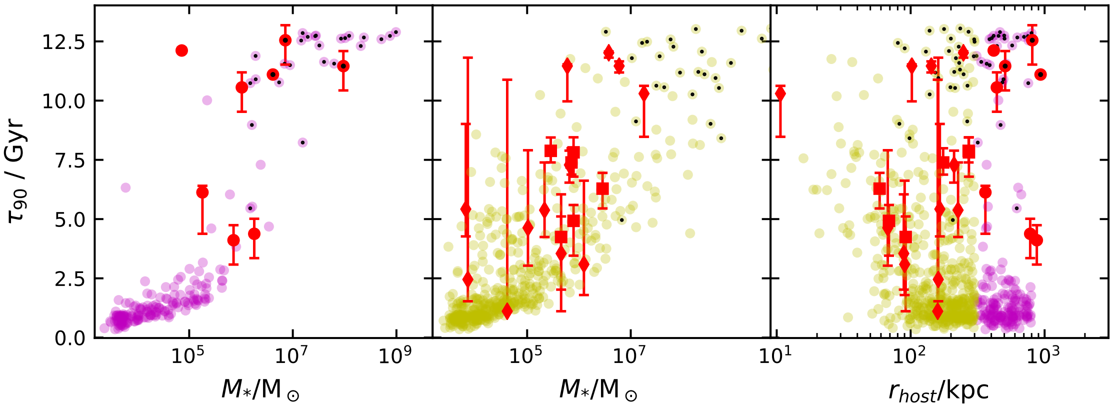

Figure A.4: As Fig. 4.6, but with Au-L3 data: The cosmic time at which galaxies have formed 90% of their stars, τ_{90}, as a function of stellar mass (left and middle panels, showing field and satellite dwarfs, respectively) and as a function of distance from the nearest primary (right-hand panel).

Bibliography

Behroozi P. S., Marchesini D., Wechsler R. H., Muzzin A., Papovich C., Stefanon M., 2013, ApJ, 777, L10

Benítez-Llambay A., Navarro J. F., Abadi M. G., Gottlöber S., Yepes G., Hoffman Y., Steinmetz M., 2015, MNRAS, 450, 4207

Benítez-Llambay A., et al., 2017, MNRAS, 465, 3913

Benson A. J., Frenk C. S., Lacey C. G., Baugh C. M., Cole S., 2002, MNRAS, 333, 177

Berger M. J., Colella P., 1989, Journal of Computational Physics, 82, 64

Boylan-Kolchin M., Bullock J. S., Kaplinghat M., 2011, MNRAS, 415, L40

Brown T. M., et al., 2014, ApJ, 796, 91

Buck T., Macciò A. V., Dutton A. A., Obreja A., Frings J., 2018, preprint, p. arXiv:1804.04667 (`arXiv:1804.04667`)

Cautun M., van de Weygaert R., Jones B. J. T., Frenk C. S., 2014, MNRAS, 441, 2923

Chabrier G., 2003, ApJ, 586, L133

Cole A. A., Weisz D. R., Dolphin A. E., Skillman E. D., McConnachie A. W., Brooks A. M., Leaman R., 2014, ApJ, 795, 54

Conroy C., 2013, Annual Review of Astronomy and Astrophysics, 51, 393

Crain R. A., et al., 2015, MNRAS, 450, 1937

Davies L. J. M., et al., 2019, MNRAS, 483, 5444

Davis M., Efstathiou G., Frenk C. S., White S. D. M., 1985, ApJ, 292, 371

Dawoodbhoy T., et al., 2018, MNRAS, 480, 1740

Digby R., et al., 2019, MNRAS, 485, 5423

Dolag K., Bartelmann M., Perrotta F., Baccigalupi C., Moscardini L., Meneghetti M., Tormen G., 2004, A&A, 416, 853

Dolphin A. E., 2002, MNRAS, 332, 91

Efstathiou G., 1992, MNRAS, 256, 43P

Emerick A., Mac Low M.-M., Grcevich J., Gatto A., 2016, ApJ, 826, 148

Fattahi A., Navarro J. F., Sawala T., Frenk C. S., Sales L. V., Oman K., Schaller M., Wang J., 2016a, arXiv e-prints, p. arXiv:1607.06479

Fattahi A., et al., 2016b, MNRAS, 457, 844

Fattahi A., Navarro J. F., Frenk C. S., Oman K. A., Sawala T., Schaller M., 2018, MNRAS, 476, 3816

Ferraro F. R., Fusi Pecci F., Tosi M., Buonanno R., 1989, MNRAS, 241, 433

Fillingham S. P., Cooper M. C., Pace A. B., Boylan-Kolchin M., Bullock J. S., Garrison- Kimmel S., Wheeler C., 2016, MNRAS, 463, 1916

Fillingham S. P., Cooper M. C., Boylan-Kolchin M., Bullock J. S., Garrison-Kimmel S., Wheeler C., 2018, MNRAS, 477, 4491

Fitts A., et al., 2017, MNRAS, 471, 3547

Gallart C., Zoccali M., Aparicio A., 2005, ARA&A, 43, 387

Gallart C., et al., 2015, ApJ, 811, L18

Garrison-Kimmel S., et al., 2019, arXiv e-prints, p. arXiv:1903.10515

Geha M., Blanton M. R., Yan R., Tinker J. L., 2012, ApJ, 757, 85

Glazer D., Rau M. M., Trac H., 2018, Research Notes of the AAS, 2, 135

Grand R. J. J., et al., 2017, MNRAS, 467, 179

Grebel E. K., 1999, in Whitelock P., Cannon R., eds, Vol. 192, The Stellar Content of Local Group Galaxies. p. 17 (`arXiv:astro-ph/9812443`)

Gunn J. E., Gott J. Richard I., 1972, ApJ, 176, 1

Guo Q., Cole S., Eke V., Frenk C., 2011, MNRAS, 417, 370

Hidalgo S. L., et al., 2011, ApJ, 730, 14

Hodge P. W., 1971, ARA&A, 9, 35

Hopkins P. F., Kereš D., Oñorbe J., Faucher-Giguère C.-A., Quataert E., Murray N., Bullock J. S., 2014, MNRAS, 445, 581

Jenkins A., 2013, MNRAS, 434, 2094

Jenkins A., Frenk C. S., White S. D. M., Colberg J. M., Cole S., Evrard A. E., Couchman H. M. P., Yoshida N., 2001, MNRAS, 321, 372

Karachentsev I. D., Makarov D. I., Kaisina E. I., 2013, AJ, 145, 101

Katz N., White S. D. M., 1993, ApJ, 412, 455

Klypin A., Kravtsov A. V., Valenzuela O., Prada F., 1999, ApJ, 522, 82

Komatsu E., et al., 2011, The Astrophysical Journal Supplement Series, 192, 18

Kravtsov A. V., Gnedin O. Y., Klypin A. A., 2004, ApJ, 609, 482

Ledinauskas E., Zubovas K., 2018, A&A, 615, A64

Mayer L., Governato F., Colpi M., Moore B., Quinn T., Wadsley J., Stadel J., Lake G., 2001, ApJ, 547, L123

McCarthy I. G., Frenk C. S., Font A. S., Lacey C. G., Bower R. G., Mitchell N. L., Balogh M. L., Theuns T., 2008, MNRAS, 383, 593

Monachesi A., Trager S. C., Lauer T. R., Hidalgo S. L., Freedman W., Dressler A., Grillmair C., Mighell K. J., 2012, ApJ, 745, 97

Monelli M., et al., 2010a, ApJ, 720, 1225

Monelli M., et al., 2010b, ApJ, 722, 1864

Moore B., Ghigna S., Governato F., Lake G., Quinn T., Stadel J., Tozzi P., 1999, ApJ, 524, L19

Murray S. G., Power C., Robotham A. S. G., 2013, MNRAS, 434, L61

Navarro J. F., Frenk C. S., White S. D. M., 1996, ApJ, 462, 563

Okamoto T., Frenk C. S., Jenkins A., Theuns T., 2010, MNRAS, 406, 208

Peñarrubia J., Navarro J. F., McConnachie A. W., 2008, ApJ, 673, 226

Peebles P. J. E., 1993, Principles of Physical Cosmology

Planck Collaboration et al., 2014, A&A, 571, A16

Planck Collaboration et al., 2018, preprint, (`arXiv:1807.06209`)

Read J. I., Iorio G., Agertz O., Fraternali F., 2017, MNRAS, 467, 2019

Sawala T., et al., 2016, MNRAS, 457, 1931

Schaye J., et al., 2015, MNRAS, 446, 521

Simpson C. M., Grand R. J. J., Gómez F. A., Marinacci F., Pakmor R., Springel V., Campbell D. J. R., Frenk C. S., 2018, MNRAS, 478, 548

Skillman E. D., et al., 2017, ApJ, 837, 102

Smith R., Choi H., Lee J., Rhee J., Sanchez-Janssen R., Yi S. K., 2016, ApJ, 833, 109

Somerville R. S., Davé R., 2015, ARA&A, 53, 51

Springel V., 2010a, ARA&A, 48, 391

Springel V., 2010b, MNRAS, 401, 791

Springel V., Yoshida N., White S. D. M., 2001, New Astronomy, 6, 79

Springel V., et al., 2005, Nature, 435, 629

Springel V., et al., 2008, MNRAS, 391, 1685

Thoul A. A., Weinberg D. H., 1996, ApJ, 465, 608

Tolstoy E., Hill V., Tosi M., 2009, ARA&A, 47, 371

Tonnesen S., Bryan G. L., 2009, ApJ, 694, 789

Tosi M., Greggio L., Focardi P., 1989, Ap&SS, 156, 295

Weisz D. R., et al., 2011, ApJ, 739, 5

Weisz D. R., Dolphin A. E., Skillman E. D., Holtzman J., Gilbert K. M., Dalcanton J. J., Williams B. F., 2014, ApJ, 789, 147

Wetzel A. R., Tollerud E. J., Weisz D. R., 2015, ApJ, 808, L27

Wetzel A. R., Hopkins P. F., Kim J.-h., Faucher-Giguère C.-A., Kereš D., Quataert E., 2016, ApJ, 827, L23

White M., 2001, A&A, 367, 27

White S. D. M., Frenk C. S., 1991, ApJ, 379, 52

White S. D. M., Rees M. J., 1978, MNRAS, 183, 341

Wright A. C., Brooks A. M., Weisz D. R., Christensen C. R., 2019, MNRAS, 482, 1176

Zolotov A., et al., 2012, ApJ, 761, 71